

AEGIS: DEMOGRAPHICS OF X-RAY AND OPTICALLY SELECTED AGNS

RENBIN YAN¹, LUIS C. HO², JEFFREY A. NEWMAN³, ALISON L. COIL^{4,5}, CHRISTOPHER N. A. WILLMER⁶, ELISE S. LAIRD⁷, ANTONIS GEORGAKAKIS⁸, JAMES AIRD⁴, PAULINE BARMBY⁹, KEVIN BUNDY^{10,11}, MICHAEL C. COOPER^{11,12}, MARC DAVIS^{10,13}, S. M. FABER¹⁴, TAOTAO FANG¹⁵, ROGER L. GRIFFITH¹⁶, ANTON M. KOEKEMOER¹⁷, DAVID C. KOO¹⁴, KIRPAL NANDRA⁷, SHINAE Q. PARK¹⁸, VICKI L. SARAJEDINI¹⁹, BENJAMIN J. WEINER⁶, S. P. WILLNER¹⁸

¹ Department of Astronomy and Astrophysics, University of Toronto, 50 St. George Street, Toronto, ON M5S 3H4, Canada; yan@astro.utoronto.ca

² The Observatories of the Carnegie Institution for Science, 813 Santa Barbara Street, Pasadena, CA 91101, USA

³ Department of Physics and Astronomy, University of Pittsburgh, 3941 O'Hara Street, Pittsburgh, PA 15260, USA

⁴ Department of Physics and Center for Astrophysics and Space Sciences, University of California, San Diego, 9500 Gilman Dr., La Jolla, CA 92093, USA

⁵ Alfred P. Sloan Foundation Fellow

⁶ Steward Observatory, University of Arizona, 933 North Cherry Avenue, Tucson, AZ 85721, USA

⁷ Astrophysics Group, Blackett Laboratory, Imperial College London, Prince Consort Rd, London SW7 2AZ, UK

⁸ National Observatory of Athens, V. Paulou and I. Metaxa, 11532, Greece

⁹ Department of Physics and Astronomy, University of Western Ontario, 1151 Richmond St., London, ON N6A 3K7, Canada

¹⁰ Department of Astronomy, University of California, Berkeley, 601 Campbell Hall, Berkeley, CA 94720, USA

¹¹ Hubble Fellow

¹² Center for Galaxy Evolution, Department of Physics and Astronomy, University of California, Irvine, CA 92697, USA

¹³ Department of Physics, University of California, Berkeley, CA 94720, USA

¹⁴ UCO/Lick Observatory, Department of Astronomy and Astrophysics, University of California, Santa Cruz, CA 95064, USA

¹⁵ Department of Physics and Astronomy, University of California, Irvine, CA 92697

¹⁶ Jet Propulsion Laboratory, California Institute of Technology, MS 169-327, 4800 Oak Grove Dr., Pasadena, CA 91109, USA

¹⁷ Space Telescope Science Institute, 3700 San Martin Drive, Baltimore, MD 21218, USA

¹⁸ Harvard-Smithsonian Center for Astrophysics, 60 Garden Street, Cambridge, MA 02138, USA and

¹⁹ Department of Astronomy, University of Florida, Gainesville, FL 32611, USA

Draft version June 28, 2018

ABSTRACT

We develop a new diagnostic method to classify galaxies into AGN hosts, star-forming galaxies, and absorption-dominated galaxies by combining the [O III]/H β ratio with rest-frame $U-B$ color. This can be used to robustly select AGNs in galaxy samples at intermediate redshifts ($z < 1$). We compare the result of this optical AGN selection with X-ray selection using a sample of 3150 galaxies with $0.3 < z < 0.8$ and $I_{\text{AB}} < 22$, selected from the DEEP2 Galaxy Redshift Survey and the All-wavelength Extended Groth Strip International Survey (AEGIS). Among the 146 X-ray sources in this sample, 58% are classified optically as emission-line AGNs, the rest as star-forming galaxies or absorption-dominated galaxies. The latter are also known as “X-ray bright, optically normal galaxies” (XBONGs). Analysis of the relationship between optical emission lines and X-ray properties shows that the completeness of optical AGN selection suffers from dependence on the star formation rate and the quality of observed spectra. It also shows that XBONGs do not appear to be a physically distinct population from other X-ray detected, emission-line AGNs. On the other hand, X-ray AGN selection also has strong bias. About 2/3 of all emission-line AGNs at $L_{\text{bol}} > 10^{44}$ ergs⁻¹ in our sample are not detected in our 200 ks *Chandra* images, most likely due to moderate or heavy absorption by gas near the AGN. The 2–7 keV detection rate of Seyfert 2s at $z \sim 0.6$ suggests that their column density distribution and Compton-thick fraction are similar to that of local Seyferts. Multiple sample selection techniques are needed to obtain as complete a sample as possible.

Subject headings: galaxies: active — galaxies: nuclei — galaxies: fundamental parameters — galaxies: Seyfert — galaxies: statistics

1. INTRODUCTION

Recently, it has been realized that nearly every massive galaxy bulge hosts a supermassive black hole (SMBH) whose mass is tightly correlated with the stellar velocity dispersion or the bulge mass (Magorrian et al. 1998; Ferrarese & Merritt 2000; Gebhardt et al. 2000). The tightness of these correlations suggests that the growth of the SMBH is physically linked with the evolution of the host galaxy. When SMBHs grow by accretion, they will appear observationally as active galactic nuclei (AGNs). A complete census of AGNs, which includes both the rare high-luminosity quasars and the more typical low-luminosity AGNs, is essential for our understanding of SMBH-galaxy co-evolution. However, such a census is not yet available beyond the local universe, primarily

due to three reasons.

First, at higher redshifts, it is difficult to spatially isolate the nuclear regions of galaxies for AGN detection. Due to the smaller apparent sizes and the fainter flux levels of distant galaxies, spatially isolated nuclear spectroscopy studies such as that of Ho et al. (1995) are not feasible at high redshifts. Using the integrated light, the detectability of AGNs at high- z unavoidably depends on host galaxy properties such as stellar mass (e.g. Moran et al. 2002) and star formation rate (SFR). All AGN selection methods have such dependences, differing in the galaxy property involved and on the level of sensitivity. This issue has not been fully addressed in the literature.

Second, there is no single method that can select a

complete sample of AGNs. In other words, no single method identifies all the AGNs found by other methods. Every method has its own bias. Besides the different dependences on host galaxy properties mentioned above, obscuration of the AGN light also causes different objects to be missed by different techniques. For example, the two methods commonly regarded as the most complete for AGN selection are optical emission-line selection and X-ray selection. Dust extinction throughout the host galaxy can dramatically reduce the observed optical emission-line luminosity and bias optical selection against edge-on disk galaxies. X-ray selection, while unaffected even by the worst levels of extinction in the host galaxy, is biased against sources in which the X-ray emission is heavily absorbed and/or Compton-scattered by dense gas clouds much closer to the central engine.

When optical AGN selection is compared with X-ray AGN selection, one type of inconsistency attracts special attention: objects generally referred to as “X-ray bright, optically normal galaxies (XBONGs)” or “optically dull” X-ray galaxies (Elvis et al. 1981; Fiore et al. 2000; Mushotzky et al. 2000; Barger et al. 2001; Comastri et al. 2002; Maiolino et al. 2003; Brusa et al. 2003; Szokoly et al. 2004; Rigby et al. 2006; Cocchia et al. 2007; Civano et al. 2007; Caccianiga et al. 2007; Trump et al. 2009b). These galaxies are bright in the X-ray, so bright that they are undoubtably AGNs. However, their optical spectra either show no emission lines at all or else emission lines having line ratios typical of star-forming galaxies. The nature of these sources has been hotly debated. Some have argued they could have an intrinsically weak narrow-line region due to large covering factor or radiatively inefficient accretion flow (Yuan & Narayan 2004). Others have suggested that the missing emission lines are due to dilution by host galaxy light (Moran et al. 2002) or extinction in the host galaxy (Rigby et al. 2006). We will investigate the nature of this population here. However, we distinguish those hosts showing star-forming-like emission-line spectra from those showing no emission lines, as the explanations are different.

Lastly, the standard method used for spectroscopic identification of AGNs is currently observationally too expensive to use for large galaxy samples at $z > 0.4$. In the local universe, the classification of AGNs and star-forming galaxies is usually achieved by the use of optical emission line ratio diagnostics (e.g., Baldwin et al. 1981; Veilleux & Osterbrock 1987). The commonly-used diagram involves two sets of line ratios: $[\text{N II}] \lambda 6583/\text{H}\alpha$ and $[\text{O III}] \lambda 5007/\text{H}\beta$ (Figure 1). However, at $z > 0.4$, $[\text{N II}]$ and $\text{H}\alpha$ are redshifted out of the optical window into the near infrared. Other available diagnostics involve either two emission lines separated by a large wavelength interval, such as $[\text{O II}] \lambda 3727/\text{H}\beta$ (Rola et al. 1997), which is sensitive to extinction and also has a limited observable redshift range, or involve the relatively weak lines, such as $[\text{N I}] \lambda 5197, 5200/\text{H}\beta$ ratio, which limit its applicability. These factors have hindered the construction of a large, complete, narrow-line AGN sample beyond $z \sim 0.4$.

This paper first establishes a new optical emission-line diagnostic method that avoids the use of $[\text{N II}]$ and $\text{H}\alpha$ lines so that we can select emission-line AGNs at redshifts beyond $z \sim 0.4$. We then make use of the rich

multi-waveband data sets enabled by the All-wavelength Extended Groth Strip International Survey (AEGIS) Collaboration and high-quality DEEP2 optical/near-IR spectra to compare the two major AGN selection methods at $0.3 < z < 0.8$: optical emission-line diagnostics and X-ray selection. In particular, we pay attention to objects that are inconsistently classified by the two methods. This paves the way to the construction of a more complete AGN sample.

As a by-product, a comparison between optical emission-line luminosities and X-ray luminosities of AGNs can also help us evaluate the absorbing column density distribution among AGNs. In particular, this helps to constrain the fraction of Compton-thick AGNs, which are required to explain the spectrum of the hard X-ray background (Gilli et al. 2007). Many studies on local AGN samples (e.g., Bassani et al. 1999; Risaliti et al. 1999) have shown that about 50% of Type 2 AGNs are Compton-thick. However, the Compton-thick fraction at higher redshift is more uncertain and is hotly debated (Daddi et al. 2007; Fiore et al. 2008; Donley et al. 2008; Treister et al. 2009; Georgantopoulos et al. 2009; Georgakakis et al. 2010; Park et al. 2010), partly due to the lack of an emission-line selected AGN sample beyond the local universe. Therefore, we hope to shed some light on this topic with our emission-line AGN sample.

Throughout the paper, we use a flat Λ CDM cosmology with $\Omega_m = 0.3$. We adopt a Hubble constant of $H_0 = 70 \text{ km s}^{-1} \text{ Mpc}^{-1}$ to compute luminosity distances. All magnitudes are expressed in the AB system.

2. DATA

2.1. X-ray imaging and optical identification

The AEGIS-X survey (Laird et al. 2009, L09 hereafter) has obtained 200 ks exposures over the entire Extended Groth Strip (EGS; Davis et al. 2007; see §2.2.1) using *Chandra* ACIS-I. It covers an area of 0.67 deg^2 and reaches a limiting flux of $5.3 \times 10^{-17} \text{ erg cm}^{-2} \text{ s}^{-1}$ in the 0.5–2 keV band and $3.8 \times 10^{-16} \text{ erg cm}^{-2} \text{ s}^{-1}$ in the 2–10 keV band at the deepest point. It provides a unique combination of depth and area, bridging the gap between the ultradeep pencil-beam surveys, such as the *Chandra* Deep Fields (CDFs) and the shallower, very large-area surveys. Its areal coverage is nearly three times larger than the CDF-North and South combined. Compared to the *Chandra* imaging in the Cosmic Evolution Survey field (*Chandra*-COSMOS; Elvis et al. 2009), our survey is slightly deeper but covers a slightly smaller area. A detailed comparison of area and flux limits among these state-of-the-art X-ray surveys is given by Elvis et al. (2009).

The data reduction and point source catalogs of AEGIS-X are presented by L09. The reduction basically followed the techniques described by Nandra et al. (2005) with new calculations of the point spread function (PSF; see L09). L09 used a wavelet detection algorithm run with a low threshold of 10^{-4} to identify candidate X-ray detections. Counts and background estimates were then extracted within an aperture corresponding to the 70% encircled energy fraction (EEF) for each candidate source and used to calculate the probability that the source is a spurious detection. All sources with a false-positive probability (p) less than 4×10^{-6} in any

of the bands (soft, hard, ultrahard, or full band) are included in the final catalog. The X-ray count rate was estimated using the 90% EEF aperture. Unlike L09, we converted the count rate to flux using a photon index of $\Gamma = 1.9$, which is more appropriate for unabsorbed sources (e.g., Nandra & Pounds 1994; Nandra et al. 1997). We also assumed this power-law spectrum to measure K -corrections from the observed X-ray flux to the rest-frame bands. Both fluxes and luminosities in this paper are reported for the rest-frame bands: 0.5–2 keV for the soft band and 2–10 keV for the hard band. The hardness ratio is defined as $HR = (H - S)/(H + S)$, where S and H are the observed counts in the 0.5–2 keV and 2–7 keV bands, respectively. The HRs were computed using a Bayesian method following Park et al. (2006) and using the BEHR package (version 07-11-2008). They are not K -corrected.

For sources detected ($p < 4 \times 10^{-6}$) in some bands but not others, if the false-positive probability (p) in an undetected band is less than 0.01, we still make a flux measurement for that band. Throughout this paper, unless otherwise noted, detection refers to having $p < 4 \times 10^{-6}$. In certain cases, we treat sources detected in other bands but having $4 \times 10^{-6} < p < 0.01$ in the 2–7 keV band as “detections” to increase the size of the sample with 2–10 keV flux measurement.

The AEGIS X-ray source catalog presented by L09 contains 1325 sources. All but 8 are inside the boundaries of the DEEP2 CFH12K photometry catalog (Coil et al. 2004). Based on a maximum-likelihood matching method (Sutherland & Saunders 1992), 895 sources are uniquely matched¹ to the DEEP2 photometric catalog with a Likelihood Ratio (LR) greater than 0.5 (L09), corresponding to a 68.0% optical identification rate. The estimated contamination rate is $\sim 6\%$. If limited to $R_{AB} < 24.1$, which is the DEEP2 survey limit, the optical identification rate is 53.5%.

2.2. Optical spectroscopy

2.2.1. DEEP2

DEEP2 is a galaxy redshift survey using the DEIMOS spectrograph on the Keck-II telescope (Davis et al. 2003; J. A. Newman et al. in prep). It covered four widely separated fields totaling 3 deg^2 on the sky down to a limiting magnitude of $R_{AB} = 24.1$. In the EGS, the survey obtained $\sim 17,775$ spectra with 12,651 yielding reliable redshifts. DEEP2 spectra typically cover approximately $6500 - -9200 \text{ \AA}$ with a resolution of $R \sim 5000$. The high resolution enables good subtraction of atmospheric emission lines and thus yields better sensitivity for line detection in the target spectra. DEEP2 employed a slit width of $1''$, which corresponds to a physical transverse scale of 7.1 kpc at $z = 0.7$.

Out of the 895 optically identified X-ray sources, 375 were observed as part of the DEEP2 survey, yielding 249 successful redshifts (66.4%) including 5 stars and 244 galaxies.

¹ Two X-ray sources in the catalog are matched to the same DEEP2 object, both with $LR > 0.5$. These two are not considered as valid matches and are removed; visual inspection of both X-ray and optical images suggests that both X-ray sources are in fact components of a single extended X-ray-emitting halo around a compact group of galaxies.

2.2.2. MMT/Hectospec follow-up

Because the sampling fraction of the DEEP2 Galaxy Redshift Survey is $\sim 50\%$ in the EGS field, and the survey began before the X-ray observations were taken, not all X-ray sources with optical counterparts were targeted for spectroscopy. We therefore obtained additional spectra using the Hectospec fiber spectrograph on MMT for as many X-ray sources with optical counterparts as possible. The observations and data reduction are described in detail by Coil et al. (2009). The spectra have a resolution of 6 \AA and cover a wavelength range of approximately $4500 - -9000 \text{ \AA}$. In total, we targeted optical counterparts for 498 X-ray sources with 288 yielding reliable redshifts, including 23 stars and 265 galaxies. The redshift success rate is a strong function of the optical magnitude (Coil et al. 2009, Figure 2).

Combining good redshifts from both surveys, out of 895 unique X-ray sources with secure optical counterparts, we have redshifts for 493 objects, including 25 stars and 468 galaxies. If we limit to the 426 sources with $I_{AB} < 22$ (the limit of our main sample used in this paper), we have 354 secure redshifts out of 388 X-ray sources targeted, corresponding to a redshift success rate of 91% and an overall completeness rate of 83%.

The rest-frame $U - B$ colors of galaxies in both spectroscopic samples were derived using the K -correction code described by Willmer et al. (2006). Stellar masses were derived by Bundy et al. (2006) from fitting spectral energy distributions to Palomar/WIRC J - and K_s -band photometry and CFH12K BRI photometry. For galaxies without Bundy et al. (2006) stellar mass estimates, we substituted the stellar masses computed from absolute M_B magnitude and rest-frame $B - V$ color using the prescription given by Bell et al. (2003) and calibrated to the Bundy et al. (2006) stellar mass scale with color- and redshift-dependent corrections (Lin et al. 2007; Weiner et al. 2009).

2.3. Emission-line measurements

We measured the emission line fluxes in each spectrum after fitting and subtracting the stellar continuum. As in Yan et al. (2006), each spectrum was fitted by a linear combination of two templates after blocking the wavelengths corresponding to emission lines. The templates were constructed using the Bruzual & Charlot (2003) stellar population synthesis code. One template features a young stellar population observed 0.3 Gyr after a 0.1 Gyr starburst with a constant SFR. The other template is an old 7 Gyr simple stellar population. Both templates are modeled assuming solar metallicity and a Salpeter initial mass function. After subtracting the stellar continua, we simply summed the flux around the emission lines and divided by the median continuum level of the original spectrum (before subtraction) in two bracketing sidebands to get equivalent widths (EWs). The definitions for the central bands and sidebands are the same as in Yan et al. (2006).

Emission line luminosity estimates require accurate flux calibration and correction for slit losses. Both are difficult to measure to better than 10% accuracy. On the other hand, broadband photometry usually has much smaller errors. Using broadband photometry, we can ap-

ply K -corrections to get the rest-frame total flux in an artificial filter corresponding to our sidebands in EW measurements. Combining this with the EW measurements yields total line flux and luminosity, avoiding the need for spectrophotometric flux calibration (Weiner et al. 2007). The accuracy of this method relies on the assumption that the emission line EW does not vary spatially within a galaxy. This assumption may not be accurate for AGNs, since the narrow-line regions subtend smaller scales than the stars in the host galaxies, leading to slightly larger [O III] EWs in the central regions of AGN hosts. However, for galaxies whose angular sizes are small compared to the seeing, the smearing of light by the atmosphere will make the emission line EW more uniform across the galaxy. X-ray sources are frequently massive galaxies. The median angular FWHM of our main sample of X-ray sources ($0.3 < z < 0.8$) in the R -band is $1''.27$, which is slightly larger than the slit width and the seeing. Therefore, this procedure will only mitigate the error caused by the slit loss but not eliminate it, and the emission line luminosity may be overestimated for AGNs. However, we expect the resulting bias and uncertainty in the emission-line luminosity to be far smaller than those in the X-ray luminosity or other uncertainties involved in the analysis, such as X-ray variability and unknown extinction corrections.

We used the DEEP2 CFH12K photometry catalog (Coil et al. 2004) and Blanton & Roweis’s (2007) *k-correct* code v4.1.4 to derive the rest-frame absolute magnitudes for the sidebands around $H\beta$ and [O III]. We then converted the magnitudes to fluxes and multiplied them by the EWs to compute the total line fluxes and luminosities. The uncertainties for the emission-line EWs were scaled up according to the differences from repeated observations, following Balogh et al. (1999) and Yan et al. (2009). The EW uncertainties are propagated into the luminosity uncertainties, along with uncertainties from photometry and K -corrections. Throughout the paper, we call an emission line *detected* if the EW is at least twice as large as its uncertainty. For non-detections, the luminosity upper limits are taken to be twice the uncertainties, i.e., 2σ .

2.4. X-ray upper limits for optical sources

Besides studying the X-ray selected sample, we have also investigated the X-ray properties of the optically selected sample. Therefore, we estimated the X-ray flux upper limits for sources not detected in X-ray. When extracting the X-ray counts at positions of the optical sources, we found that many of them have significant counts above the background. In many cases, the probability that the counts arise from background fluctuation is less than 0.1%. The number of such cases is much higher than the expected number of false-positive cases, suggesting that many of them could be truly associated with the optical sources. It is very tempting to include them as X-ray detections to increase the sample size. However, because the X-ray PSF is usually larger than the PSF in the optical images, the X-ray flux could come from other untargetted galaxies nearby or even galaxies beyond the optical photometry detection threshold. Therefore, we only quote X-ray flux upper limits for these sources although the X-ray flux could be significant.

We estimate the X-ray flux upper limits using the

Bayesian method (Helene 1984; Kraft et al. 1991, L09). However, unlike L09, who used a power-law prior for the source flux distribution, we used a constant, non-negative prior (Kraft et al. 1991) with minimal assumptions made about the source flux distribution. This gives more conservative upper limits than the power-law prior. As we do not require an X-ray detection, we do not suffer from Eddington bias. Our upper limits correspond to the 95% confidence limit (2σ). In detail, the method applies the Bayes’ theorem,

$$P(s|N, b) \propto L(N|s, b)\pi(s), \quad (1)$$

where $L(N|s, b)$ is the conditional probability of observing N counts given the expected source counts s and expected background counts b ; it follows the Poisson distribution,

$$L(N|s, b) = \frac{(s+b)^N}{N!} e^{-(s+b)}. \quad (2)$$

$\pi(s)$ is the prior probability distribution of the expected source counts; following Kraft et al. (1991), we adopt a step function for $\pi(s)$, which is a constant when $s > 0$ and is zero otherwise. Bayes’ theorem yields the posterior distribution function, $P(s|N, b)$, for the expected source counts given the observed counts and the expected background.

Here we assume that the error in the estimated background is small, thus b is known. For each source, the total counts were estimated in an elliptical aperture that contains 70% of the energy in the simulated PSF. The aperture was obtained using the PSF look-up table provided by L09. The mean background counts for each source were derived the same way as by L09 but were estimated for the aperture with EEF (enclosed energy fraction) of 70% instead of the 90% EEF aperture. Given the observed counts and the expected background counts, we estimated the upper limit of the source counts using the formulae given in Kraft et al. (1991). The count limit was then converted to a flux limit and K -corrected by assuming a power-law photon index of $\Gamma = 1.9$.

3. A NEW EMISSION LINE RATIO DIAGNOSTIC

3.1. The traditional method

The classification of AGN and star-forming galaxies is usually achieved by the use of optical emission line ratio diagnostics (Baldwin et al. 1981, hereafter BPT; Veilleux & Osterbrock 1987). One most commonly-used diagram involves two sets of line ratios: [N II] $\lambda 6583/H\alpha$ and [O III] $\lambda 5007/H\beta$ (Figure 1). In such a diagram, a.k.a. the BPT diagram, the star-forming galaxies populate a sequence from the upper left to the lower center which is the consequence of a correlation between metallicity and ionization parameter. With increasing metallicity, the ionization parameter and hence [O III]/ $H\beta$ decrease. Galaxies to the right and upper right of the star-forming sequence are AGN hosts, which include Seyferts ([O III]/ $H\beta > 3$) and low-ionization nuclear emission-line regions (LINERs, [O III]/ $H\beta < 3$). AGNs produce higher [O III]/ $H\beta$ and [N II]/ $H\alpha$ ratios than star-forming galaxies because of two reasons. First, AGNs have much higher ionization parameters so that they are capable of doubly ionizing more oxygen atoms. Secondly, their photons are more energetic than those from massive stars

and can generate a more extended partially ionized region, where [N II] is produced. The exact line ratios depend on the elemental abundances and the strength and shape of the ionizing spectra. For a more detailed discussion, see Stasińska et al. (2006). Nonetheless, the line ratio diagnostics provide a powerful way to distinguish AGN-dominated galaxies from star-formation-dominated galaxies.

Two empirical demarcations are commonly used for defining AGNs and illustrated in Figure 1. Kewley et al. (2001) provided a demarcation based on extreme starburst models. It is a fairly conservative limit for defining AGNs. Kauffmann et al. (2003) proposed a more inclusive demarcation. Galaxies that lie between the two demarcations are often referred to as composite galaxies that have both AGN and star formation. Since SDSS fiber apertures include both the nucleus and the host galaxy, a lot of galaxies in this region are probably composites. However, this name is misleading in two ways. First, galaxies outside this intermediate region could also be composite galaxies. Second, some galaxies inside this region do not have to be composites, and there are evidences against the composite assumption. Using *HST*/STIS observations, Shields et al. (2007) showed that in many such objects identified in the Palomar survey (Ho et al. 1995), the line ratios do not become more AGN-like on smaller apertures (10–20 pc), contrary to the expectation for composites that smaller apertures will include less star formation contribution. Therefore, we choose to refer to the region in between the two demarcations as the “Transition Region”. For the regions above and below, we refer to them as “AGN” and “star-forming”, respectively. Note, our definition of “Transition Region” is different from that of the “Transition Objects” as defined by Ho et al. (1997) based on a set of line ratios including [O I]/H α and using nuclear spectra.

3.2. Our new diagnostic method

As mentioned in §1, it is observationally very expensive to apply the traditional AGN diagnostics at $z > 0.4$ due to the inaccessibility of [N II] and H α in the visible window. Weiner et al. (2007) proposed a “pseudo-BPT” diagram using rest-frame *H*-band magnitude, M_H , to replace the [N II]/H α ratio. For star-forming galaxies, M_H , a proxy for stellar mass, correlates with the metallicity-indicating [N II]/H α ratio. Thus, this method can distinguish Seyferts in relatively massive hosts from low mass, low metallicity star-forming galaxies. However, because the correlation between stellar mass and [N II]/H α breaks down for AGN host galaxies, the separation between star-forming galaxies and AGNs is not very clean. Inspired by Weiner et al. (2007), we propose a more effective classification method employing the optical $U - B$ color of galaxies in place of the [N II]/H α ratio. Below we first demonstrate this method using a galaxy sample from SDSS; then we explain why it works and why color works better than stellar mass.

The galaxy sample used in Fig. 1 is selected from the Sloan Digital Sky Survey (SDSS, York et al. 2000) — Data Release Six (Adelman-McCarthy et al. 2008) by requiring $0.05 < z < 0.1$, $r < 19.77$, and all four emission lines detected at more than 2σ significance. The emission lines are measured in the same way as by Yan et al.

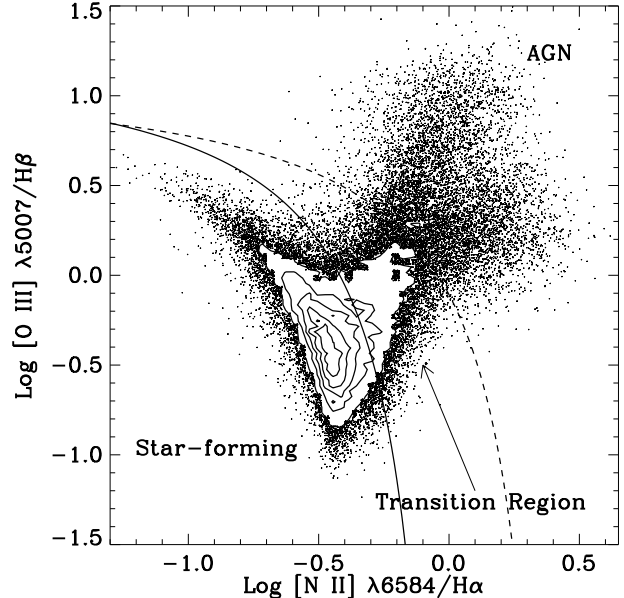


FIG. 1.— Most commonly used line ratio diagnostic diagram (BPT) for a sample of the Sloan Digital Sky Survey (SDSS) galaxies with $0.05 < z < 0.1$, $r < 19.77$, and all four emission lines detected at $>2\sigma$ level. The two curves indicate the AGN demarcations of Kauffmann et al. (2003) (solid line) and Kewley et al. (2001) (dashed line). We use these demarcations to divide galaxies into three groups: AGN hosts (upper right), star-forming galaxies (lower left), and transition region (middle). Their distributions in our new diagnostic diagram are shown in Fig. 2.

(2006). As discussed above, we separate this sample into three classes: star-forming galaxies, transition region galaxies, and AGNs. Figure 2 replaces the horizontal axis with the rest-frame $U - B$ color.² The AGN hosts (panel c) are still in the upper right portion of the diagram, separated from the star-forming galaxies. The transition region galaxies overlap primarily with the star-forming galaxies in $U - B$ color. If we limit attention to pure AGNs, the $U - B$ color provides an effective alternative to the [N II]/H α ratio for selecting a sample.

In choosing an empirical demarcation in the new diagnostic diagram, our preference is to limit contamination to the AGN sample. This new method certainly cannot select all galaxies containing AGNs down to the demarcation of Kauffmann et al. (2003) without being heavily contaminated by star-forming galaxies. We thus place the line just above the area populated by pure star-forming galaxies, which still allows us to retain most AGNs classified by the Kewley et al. (2001) limit. The demarcation we use is given by

$$\log([\text{O III}]/\text{H}\beta) > \max\{1.4 - 1.2(U - B), -0.1\}, \quad (3)$$

where $\max\{a, b\}$ denotes the greater value of a and b , and $U - B$ is the rest-frame color in the AB magnitude system. This is illustrated by the lines in Fig. 2. The horizontal cut is a bit arbitrary: red galaxies with low [O III]/H β ratio could be either transition region objects or very dusty star-forming galaxies. There are relatively few of them. We leave the fine tuning for future work.

² The rest-frame $U - B$ color for SDSS galaxies was derived using Blanton & Roweis (2007)’s *k-correct* code v4.1.4.

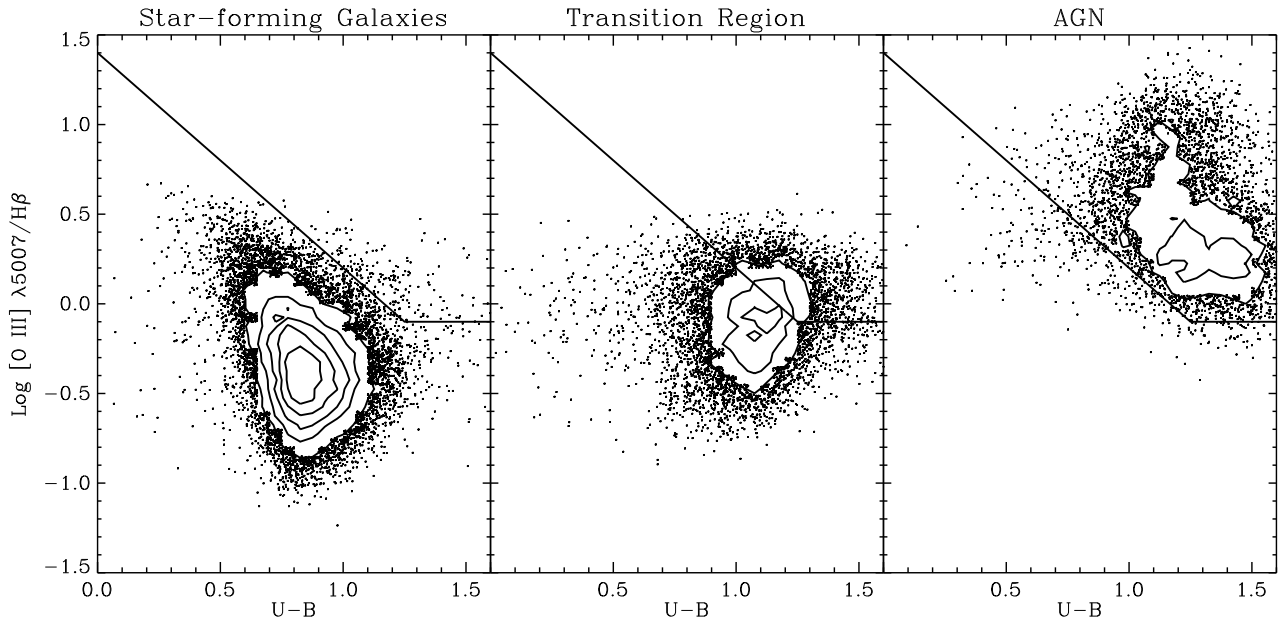


FIG. 2.— Same sample of galaxies as in Fig. 1, but replacing $[\text{N II}]/\text{H}\alpha$ ratio on the horizontal axis with the rest-frame $U - B$ color. The three panels are for (a) star-forming galaxies, (b) transition region galaxies, and (c) AGN hosts, classified according to their positions in Fig. 1. The solid lines indicate our empirical demarcation for AGN selection, which removes nearly all pure star-forming galaxies (only 0.66% of all star-forming galaxies in the sample cross this line).

With this demarcation (Eqn. 3), we find 95.7% (7138 out of 7459) of the AGNs selected using the Kewley et al. (2001) demarcation are still classified as AGNs using the new method. If we include all objects in the transition region as AGN hosts, the completeness of the new method drops to 54.3% (9757 out of 17969). About 1.9% (190 out of 9947) of the new “AGNs” were classified as star-forming galaxies under the old method; these we consider contamination.

3.3. The principle and the bias

The new classification method is based on the fact that nearly all BPT-identified AGNs are found in red galaxies or those with intermediate colors between red and blue (hereafter, green galaxies), but hardly any are found in very blue galaxies. There are several reasons. First, blue galaxies are less massive and have smaller bulge-to-disk ratios than red galaxies. Smaller bulges host smaller black holes (Magorrian et al. 1998; McLure et al. 2006). The bluer a galaxy is, the less massive its black hole is, and at a fixed Eddington ratio, the less luminous the AGN will be. Thus, a lower fraction of the AGNs in blue galaxies will be found above the observational flux threshold than those in green or red galaxies. Second, star formation in blue galaxies could overwhelm weak or moderate AGNs so that the combined line ratios still put them in the star-forming sequence on the BPT diagram. Both of these effects tend to hide AGNs in blue galaxies. There may also be other physical effects that we do not yet understand. Nonetheless, this observational fact allows us to use host galaxy color to reproduce the BPT selection of AGNs.

On the other hand, nearly all red/green galaxies that have high $[\text{O III}]/\text{H}\beta$ ratios are found to be AGNs. This is because high $[\text{O III}]/\text{H}\beta$ ratios require high ionization parameters which are produced in two types of sources:

AGN and low-metallicity hot stars. Low-metallicity stars are only forming in very blue star-forming galaxies. Therefore, when limited to red or green galaxies, the high $[\text{O III}]/\text{H}\beta$ ratios have to be due to an AGN.

Therefore, the rest-frame $U - B$ color can be used to track AGN activity in a similar fashion as the BPT diagram, because it correlates positively with the bulge mass and metallicity, and correlates negatively with the star formation rate. Other colors or spectral index (e.g., $D_n(4000)$) could also be employed provided they satisfy these criteria.

What kind of AGNs will our method miss? First of all, this method is not intended to select broad-line AGNs (Type 1) in which the broadband color is not dominated by the host galaxy. Among narrow-line AGNs, one might worry that this method will miss those Seyferts with high $L_{[\text{O III}]} / M_{\text{BH}}$ which are shown to live in blue star-forming galaxies (Kauffmann et al. 2007). However, since our demarcation is tilted, we will not miss the majority of these Seyferts: their “blue” colors are redder than our limit. We tested this using our SDSS sample described in §3.2. We derived $L_{[\text{O III}]} / M_{\text{BH}}$ following Kauffmann et al. (2007) and selected the 5% of AGNs (defined using the Kewley demarcation) with the highest values of $L_{[\text{O III}]} / M_{\text{BH}}$, 77% of these are still classified as AGNs in our new diagram. This fraction is lower than that for all AGNs since these galaxies do fall on the blue edge of the AGN sample. Nonetheless, our new method can recover the great majority of them.

LINERs will be missed by this method if they live in blue galaxies, which will make them LINER-star-forming composites. On the BPT diagram, they will belong to the transition region. We will not be complete for this category. The fraction missed depends on where we put the demarcation and which method we regard as giving

the “correct” classification for each galaxy, if it can be well defined. By lowering the demarcation to include more transition region galaxies, we would have more “contaminations” from the BPT star-forming sequence. However, some of these “contaminations” could also be AGN-SF composites. Regarding to SF-AGN composites, our method has a similar selection bias as the BPT diagrams, but with different detailed dependences.

Locally, we do not find low-metallicity AGNs (Stasińska et al. 2006). If there exist at higher- z , they could be missed by both our methods and the traditional BPT diagram.

There is also much evidence now suggesting that many luminous AGNs have previously had a star formation episode (Kauffmann et al. 2003; Jahnke et al. 2004; Sánchez et al. 2004; Silverman et al. 2008), so they have bluer host galaxies than their inactive counterparts. Would we miss the AGNs in these galaxies? The answer is “No”. Most post-starbursts in SDSS and DEEP2 have redder $U - B$ colors than the median star-forming galaxy (Yan et al. 2009), because the U band covers the blue side of the Balmer break. We therefore do not expect to miss AGNs in most post-starbursts, at least up to $z \sim 0.8$.

The principal advantage of this method is that it requires fewer emission lines than the traditional one. Hence, it can be applied to higher redshift galaxies and suffers less from incompleteness due to missing line detections, especially in low signal-to-noise (S/N) spectra.

3.4. Comparison to other methods

One might expect that stellar masses would perform equally well as a replacement for $[\text{N II}]/\text{H}\alpha$. However, this is not the case. Figure 3 shows how mass compares with rest-frame $U - B$ color in their correlations with $[\text{N II}]/\text{H}\alpha$. The sample used is selected from SDSS DR6 with $0.02 < z < 0.1$, $M_* > 10^9 M_\odot$, and by requiring both $[\text{N II}]$ and $\text{H}\alpha$ are detected at more than 2σ significance. The stellar masses are derived as a by-product in K -correction (Blanton & Roweis 2007). We imposed a redshift-dependent stellar mass cut so that at all redshifts the sample is complete to a certain stellar mass limit for all colors. With this cut, for each galaxy, we computed the maximum volume over which a galaxy with that stellar mass would be included in the sample, V_{max} . Figure 3 plots the $1/V_{\text{max}}$ -weighted distribution in $[\text{N II}]/\text{H}\alpha$ versus M_* and $[\text{N II}]/\text{H}\alpha$ versus $U - B$ spaces. These reflect the distributions of all galaxies in a volume-limited sample down to $M_* > 10^9 M_\odot$ that have a reliable $[\text{N II}]/\text{H}\alpha$ measurement.

In Figure 3, the rest-frame $U - B$ color shows a much better correlation with $[\text{N II}]/\text{H}\alpha$ ratio than stellar mass does. The difference is especially dramatic at $\log([\text{N II}]/\text{H}\alpha) > -0.2$, where the trend for stellar mass becomes horizontal. These high $[\text{N II}]/\text{H}\alpha$ galaxies are mostly AGN-host galaxies that are old and have very low or zero SFRs (as indicated by their red colors). Both $[\text{N II}]/\text{H}\alpha$ and color increase with metallicity in passively evolving galaxies (see Groves et al. 2004 for the dependence of $[\text{N II}]/\text{H}\alpha$ on metallicity for AGNs), and hence they remain correlated as metallicity changes. However, although stellar mass correlates with metallicity for star-forming galaxies, stellar mass stops growing once the star formation stops. Thus, it no longer correlates with the

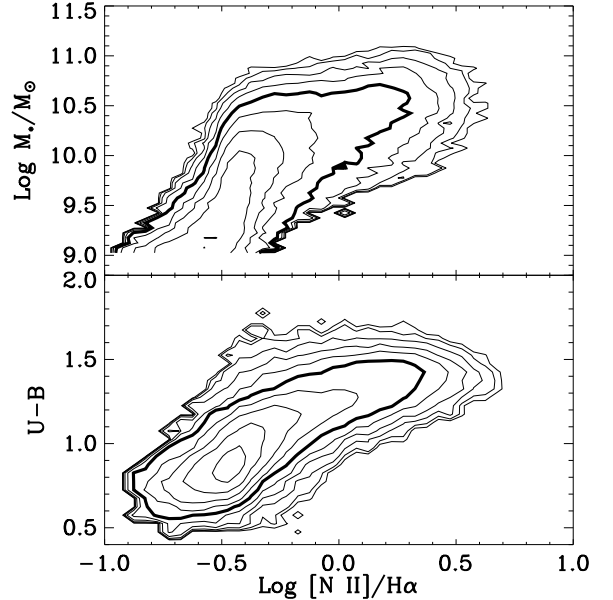


FIG. 3.— Correlations between $[\text{N II}]/\text{H}\alpha$ and M_* (upper panel) and between $[\text{N II}]/\text{H}\alpha$ and $U - B$ (lower panel). The sample is from the SDSS with selection described in §3.4. The contours denote equal density levels, $1/V_{\text{max}}$ weighted so they reflect the distribution of a volume-limited sample. The contours are logarithmically spaced with each level inward representing a factor of two increment in number density. The highlighted thicker contour encloses 88% (upper panel) or 90% (lower panel) of all galaxies in a volume-limited sample.

$[\text{N II}]$ abundance or $[\text{N II}]/\text{H}\alpha$ ratio. Therefore, color provides a better alternative to $[\text{N II}]/\text{H}\alpha$ than stellar mass does.

Lamareille et al. (2004; 2010) investigated the use of $[\text{O II}] \lambda 3727/\text{H}\beta$ EW ratio as an alternative to $[\text{N II}]/\text{H}\alpha$. This enables the application to redshifts as high as our method, though it also requires that $[\text{O II}]$ lines are covered in the spectra. This method also has troubles differentiating the transition region from the star-forming galaxies. Under their method, 84.5% of all Seyferts and LINERs (above the Kewley et al. 2001 demarcation) are classified as AGNs, smaller than our completeness of 95.7%. The contamination from the star-forming sequence (below the Kauffmann et al. 2003 demarcation) to the AGN category is 2.6%, larger than our number of 1.9%.

3.5. Intermediate- z test

The SDSS galaxy sample we used is at $z < 0.1$. We have shown above that the new method works at this redshift. Does it still work at higher redshifts?

We can test our new AGN/star-forming classification method between redshifts 0.2 and 0.4, where the traditional line ratio diagnostics are still available within the optical window. We used the spectroscopic data obtained in the EGS by the DEEP2 survey and with Hectospec to test the method. The results are shown in Fig. 4. The traditional method identified 40 emission line AGNs that are above the Kewley et al. (2001) demarcation.³ The

³ For four objects near the demarcation with arrows pointing across it, the limits on line ratios strongly suggest that they belong

new method identified 36 of them and missed 4, corresponding to a 90% completeness. It also picked up 8 objects from the transition region with no contamination from star-forming galaxies. It is also encouraging to note that as about many X-ray sources (11 out of 12) are identified as AGNs in the new diagram as in the traditional diagram (10 out of 12).

Because galaxies are bluer at higher redshift (Blanton 2006), in principle, our demarcation should shift blueward slightly. By comparing the color–magnitude diagram of the DEEP2 sample at $z \sim 0.9$ with that of an SDSS galaxy sample at $z \sim 0.1$, we found the division between red and blue galaxies shifts by 0.14 mag in $U - B$ between these redshifts (Cooper et al. 2008; Yan et al. 2009), which is consistent with the passive evolution prediction (van Dokkum & Franx 2001). The corresponding shift between $z = 0.3$ and $z = 0.1$ is about 0.04. For the sample we will discuss later, which has $0.3 < z < 0.8$ and a median redshift of $z \sim 0.55$, the shift is about 0.08 from $z \sim 0.1$. These shifts are quite small and insignificant for our results. Considering our sample covers a wide redshift range, for simplicity, we do not apply these shifts.

4. X-RAY SELECTION VS. OPTICAL SELECTION

A commonly used method to identify X-ray AGNs is to use a pure luminosity cut of $L_{2-10\text{keV}} > 10^{42} \text{ erg s}^{-1}$. This is a very conservative threshold which is based on the fact that no local star-forming galaxies have X-ray luminosity above it⁴. However, lower luminosity sources could also be bona fide AGNs, which are equally, if not more, interesting. The advantage of a selection based on X-ray luminosity is its rough correspondence to a bolometric luminosity selection (Elvis et al. 1994). However, this can be compromised by intrinsic absorption of the X-ray luminosity. Below, we compare the X-ray selection to optical emission line selection in the DEEP2 and Hectospec sample.

We limited our sample to objects that have both [O III] and $H\beta$ covered in the spectra, which corresponds roughly to a redshift range of $0.3 < z < 0.8$. The redshift range is approximate due to the slightly varying wavelength coverage of the DEEP2 spectra. We made a magnitude cut at $I_{\text{AB}} < 22$ so that our redshift success rate is above 90% for both red and blue galaxies, and the spectra have a sufficient S/N for stellar continuum subtraction. As shown in Figure 5, few X-ray sources at $0.3 < z < 0.8$ are excluded by this cut. To summarize, all sources in our sample have to satisfy all of the following criteria:

1. be within the X-ray footprint;
2. $I_{\text{AB}} < 22$;
3. have reliable redshifts from either the DEEP2 survey or the Hectospec follow-up;
4. have [O III] and $H\beta$ well covered in the spectra, not badly affected by CCD gaps or very bright sky lines;

to the category across the demarcation. Thus, we assigned them those classifications.

⁴ Using the calibration by Ranalli et al. (2003), one would need an SFR of $200 M_{\odot} \text{ yr}^{-1}$ to produce enough X-ray luminosity from non-AGN sources to cross this threshold.

5. $z > 0.3$.

In total, there are 3150 galaxies and 146 X-ray sources in this sample.

In our analysis, we primarily focus on Type 2 AGNs since their comoving number density is much higher than that of Type 1 AGNs, and the latter are usually identified easily in both optical spectra and X-ray data. However, we will use Type 1 AGNs as a reference sample. We visually identified Type 1 AGN candidates among the spectra from DEEP2 and the MMT/Hectospec follow-up survey. We measured the FWHM of the broad lines ($H\alpha$, $H\beta$, or $Mg \text{ II}$) and classified those with FWHM greater than 1000 km s^{-1} as Type 1 AGNs. There are 21 Type 1 AGNs in our sample. All but one are detected in the X-ray. The one undetected object is not far from the detection threshold in the hard band, with a false-positive probability of 1.8×10^{-3} .

In Figure 6, we present the new emission-line diagnostic diagram for all non-Type-1 galaxies in our sample. The distribution is similar to that at $0.2 < z < 0.4$ (right panel of Fig. 4). For galaxies with either [O III] or $H\beta$ undetected, we place them at their lower or upper limits for [O III]/ $H\beta$. In 89% of such cases (726 out of 815), the upper limits on the undetected lines are tight enough that they do not introduce any ambiguity in the classifications of the objects. The remaining 11% are classified as “ambiguous”, which represents 3% of our sample and can be safely neglected. Figure 6 also plots those galaxies with neither [O III] nor $H\beta$ detected at the bottom. Effectively, we classify all galaxies into three main categories: star-forming, AGNs, and quiescent. The X-ray detected sources (excluding Type 1 AGNs) are found in all three categories. We use solid symbols to denote sources with $L_X(2-10 \text{ keV}) > 10^{42} \text{ erg s}^{-1}$ and open symbols to denote fainter sources. The fainter sources either have a detected $L_X(2-10 \text{ keV}) > 10^{41} \text{ erg s}^{-1}$, or, in the cases of hard band undetection, have a minimum $L_X(2-10 \text{ keV})$ extrapolated (assuming $\Gamma \leq 1.9$) from the 0.5–2 keV band greater than $10^{41} \text{ erg s}^{-1}$.

The differences between the two selection methods are apparent in this figure. First, consider the optically selected Type 2 AGNs: these are points above the demarcation. Many of them (78% of all optically selected Type 2 AGNs) are not detected in X-rays. Some are detected but are fainter than the commonly used $10^{42} \text{ erg s}^{-1}$ threshold. The majority (51%) of non-Type-1 X-ray sources with $L_X(2-10 \text{ keV}) > 10^{42} \text{ erg s}^{-1}$ are also optically classified as AGNs. However, 22% of them are found in the star-forming part of the line ratio diagram and 25% are found to have no detectable line emission. As mentioned in §1, these cases are often referred to as XBONGs or optically-dull X-ray galaxies. Often, the term XBONG is used to refer both to galaxies with no detectable line emission and to those with line ratios of typical star-forming galaxies. We suggest treating these two cases separately as the galaxies are two distinct types; in the remainder of this paper, we only use XBONG to refer to the class with no detectable line emission, and thus our XBONGs are nearly all red-sequence galaxies.

To understand the reason for the discrepancy between optical selection and X-ray selection, we investigate a few classes of objects, grouped according to the differences in X-ray and optical classifications. To simplify

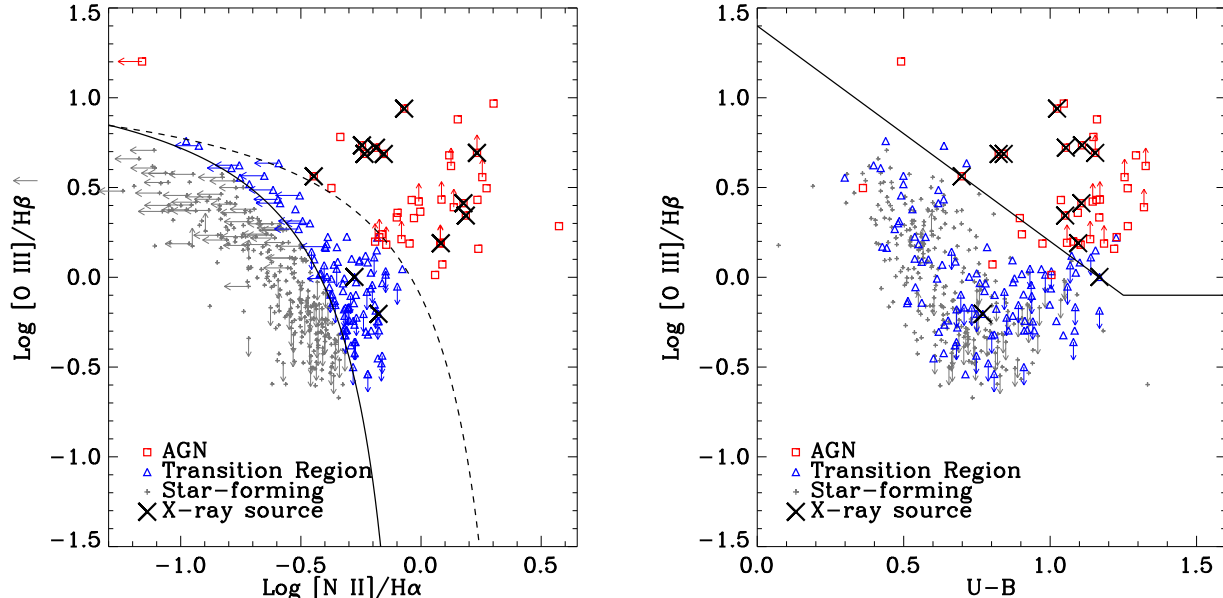


FIG. 4.— Left: standard line ratio diagnostic diagram for a sample of sources in the EGS with $0.2 < z < 0.4$. Arrows indicate the 2σ upper and lower limits for galaxies in which one of the four lines is not significantly detected. The solid and dashed curves show the demarcation used by Kauffmann et al. (2003) and Kewley et al. (2001) to separate AGN hosts from star-forming galaxies. We use the two curves to classify all galaxies into three categories: red squares indicate AGN host galaxies; small gray crosses are star-forming galaxies; and blue triangles are galaxies in between, which is usually considered as composite objects. Large dark crosses indicate sources detected in the X-ray. Right: the same galaxies now plotted on the $U - B$ vs. $[\text{O III}]/\text{H}\beta$ diagram. The AGN hosts are still at the upper right portion, separated from star-forming galaxies. The solid lines mark our empirical cuts, which were designed on the basis of lower-redshift, SDSS data.

things, we do not separate the bright and faint X-ray sources into two separate categories, since the luminosity threshold is somewhat arbitrary. We have three optical classifications—AGN, SF, and quiescent—and two X-ray classifications—detections and non-detections.

First, we will consider the objects that are classified as AGNs by the optical selection and are detected in X-ray. For brevity, we will call them “unambiguous AGNs”. Second, we will discuss X-ray detected sources that are found in the star-forming branch of our diagnostic diagram. Following Moran et al. (1996) and Levenson et al. (2001), we call them “X-ray-loud composite galaxies”, reflecting their AGN-star-forming composite nature, as we will show below. Third, we will investigate X-ray sources with no detectable line emission (XBONGs). Lastly, we will discuss optically selected AGNs with no X-ray detection, which we refer to as “optical-only AGNs”. We will use these names for each class throughout the remainder of this paper. Their definitions are summarized in Table 1, along with the number of objects in each class. Note, because of the preferential follow-up of the X-ray sources, the numbers in this table should not be used to estimate the fraction of emission-line AGNs that are detected in the X-ray. For that analysis, we limit the sample to only sources targeted in the DEEP2 survey, where no preference was given to X-ray sources.

As will be shown below, the union of X-ray selected AGNs and optically selected AGNs provides a much more complete AGN sample. Table 4 lists the IDs, coordinates, redshifts, optical colors, emission line properties, and the classifications of all the X-ray sources and the optical-only AGNs in our sample, along with Type 1 AGNs.

4.1. Unambiguous AGNs

Most (83%) optically classified AGNs that are also detected in X-rays have $L_X(2-10 \text{ keV}) > 10^{42} \text{ erg s}^{-1}$, which confirms their identity as AGNs. The correlations between the emission line and X-ray luminosities of this population establish prototype relations for AGNs. Both $[\text{O III}]$ and hard X-ray are good indicators for AGN bolometric luminosity (Heckman et al. 2004 for $[\text{O III}]$; Elvis et al. 1994 for X-ray). Because $[\text{O III}]$ originates from the narrow-line region, which is outside the obscuring dusty torus, it is usually regarded as an isotropic luminosity indicator. While X-rays can penetrate dust easily, they can be absorbed by a high column density of neutral gas in the torus. Among Type 1 AGNs, for which we have an unobstructed view of the accretion disk, X-ray luminosity is found to correlate with $[\text{O III}]$ luminosity (Mulchaey et al. 1994; Heckman et al. 2005). Therefore, comparing X-ray with $[\text{O III}]$ can reveal the level of X-ray absorption (Maiolino et al. 1998; Bassani et al. 1999).

Figure 7 compares $[\text{O III}]$ emission with X-ray in both flux and luminosity. Type 1 AGNs have a slightly larger median $\log(L_X(2-10 \text{ keV})/L_{[\text{O III}]})$ ratio (1.83 dex) and a narrower distribution than our Type 2 AGNs (median=1.42 dex, see Table 2). However, the $L_X(2-10 \text{ keV})/L_{[\text{O III}]}$ difference between Type 1 and Type 2 AGNs depends on how the sample is selected. Heckman et al. (2005) showed that in a hard-X-ray-selected sample of local AGNs, Type 1 and Type 2 AGNs exhibit $L_X(2-10 \text{ keV})/L_{[\text{O III}]}$ ratios indistinguishable from each other. However, in a sample selected by $[\text{O III}]$ luminosity, many Type 2’s can be present with low X-ray

TABLE 1
CLASSIFICATION DEFINITIONS FOR NON-TYPE-1 OBJECTS

Emission Line (3129)	X-ray Detected (126)	X-ray Undetected (3003)
AGN (291)	Unambiguous AGNs (64)	Optical-only AGNs (227)
SF (1799)	X-ray-loud composite galaxies (28)	
Quiescent (950)	XBONGs (32)	
Ambiguous (89)	Ambiguous (2)	

NOTE. — The numbers in parentheses indicate the sample size in each class.

TABLE 2
MEDIAN $\log L_X(2-10 \text{ keV})/L_{[\text{O III}]}$ RATIOS FOR UNAMBIGUOUS AGNS

Class	HX-selected		[O III]-selected	
	Our Sample	Heckman et al. (2005)	LaMassa et al. (2009)	
Type 1	1.83 (0.29)	1.69 (0.41)		
Type 2	1.42 (0.50)	0.68 (1.16)	0.46 (1.01)	
Combined	1.57 (0.53)	1.22 (1.01)		

NOTE. — Numbers in parentheses are the scaled median absolute deviations S_{MAD} of each sample. Median absolute deviation (MAD) is a robust estimator of distribution width for small samples. We follow Beers et al. (1990) to define $S_{\text{MAD}} = \text{MAD}/0.6745$, which is 1 for a normal distribution with standard deviation = 1. Statistics from Heckman et al. (2005) and LaMassa et al. (2009) have been computed from their data tables.

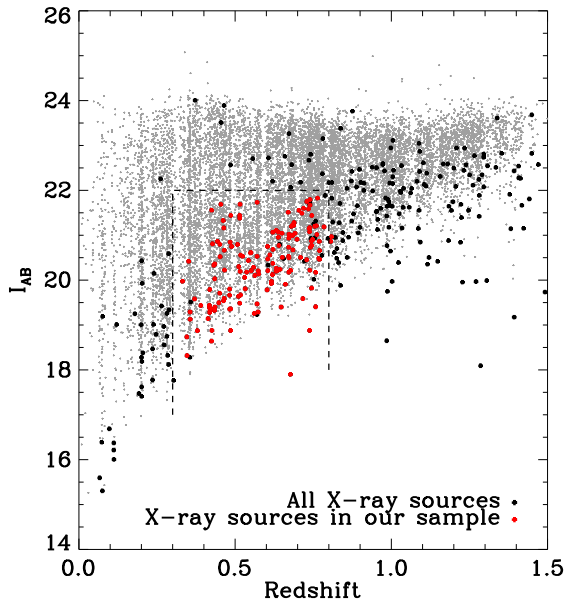


FIG. 5.— Magnitude and redshift distribution of X-ray sources (large points) that have optical counterparts and successful redshifts from the DEEP2 survey and/or the Hectospec follow-up program, compared with the overall distribution of galaxies (small gray points) with redshift successfully obtained in these two surveys. The red points are X-ray sources in our sample. The dashed lines indicate the magnitude limit and the approximate redshift limits. The latter is approximate due to the slightly varying wavelength coverages of DEEP2 spectra. Objects are rejected from the sample if their spectra do not cover both [O III] and $H\beta$, which could also be due to CCD gaps, bad columns, etc. We also exclude all objects at $z < 0.3$.

luminosity, presumably due to absorption. The Type 1 AGNs then have a median ratio much larger than that of Type 2 and have significantly less variation in the ratio than Type 2 AGNs. The unambiguous AGNs are effectively a hard-X-ray-selected sample; there is a small difference between Type 1 and Type 2 but not nearly as

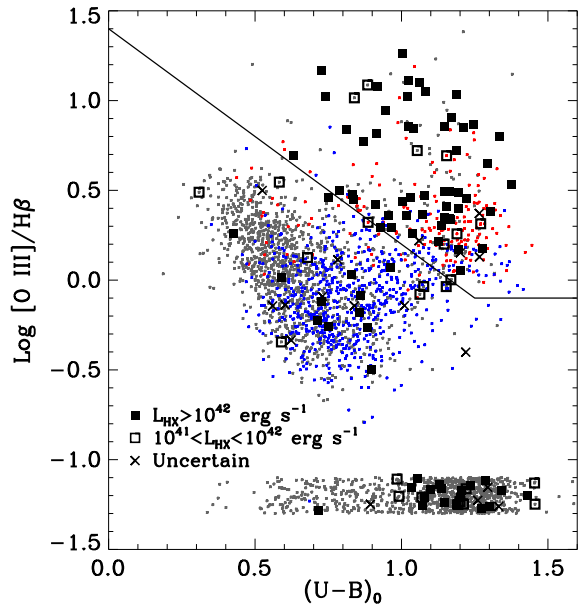


FIG. 6.— New emission-line diagnostic diagram for DEEP2 galaxies with $0.3 < z < 0.8$. The solid line shows the proposed demarcation between star-forming galaxies (below and to the left) and AGNs (above and to the right). Galaxies with either [O III] or $H\beta$ undetected are placed at their 2σ upper (blue points) or lower (red points) limits, respectively (arrows are omitted for clarity). In nearly all cases, these line ratio limits do not affect the classification of objects. Quiescent galaxies without detectable emission lines are also shown at the bottom. X-ray sources, which are found in all three categories, are marked as large symbols. Solid squares are bright sources with $L_{2-10\text{keV}} > 10^{42} \text{ erg s}^{-1}$; open squares are faint sources with $L_{2-10\text{keV}} < 10^{42} \text{ erg s}^{-1}$; and crosses are X-ray sources with uncertain luminosity classes—they are usually undetected in the hard band. Only objects in the first category may be definitely classified as AGNs, though many in the second class will be AGNs.

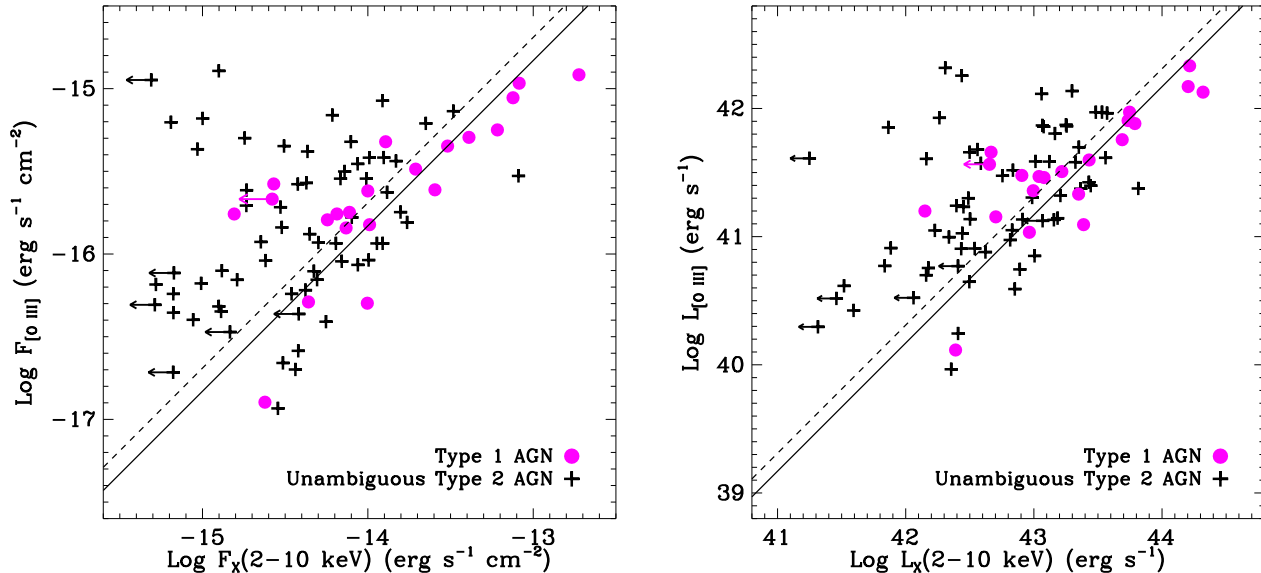


FIG. 7.— Left: $[\text{O III}]$ line flux versus 2–10 keV X-ray flux for unambiguous AGNs, which are X-ray sources that are classified as AGNs by emission line diagnostics. Type 1 AGNs are also shown here as solid magenta circles. The dashed line indicates the median ratio found by Heckman et al. (2005) for Type 1 AGNs. The solid line indicates the median ratio in our Type 1 sample. Right: similar to the left panel but comparing luminosity rather than observed flux.

large as the difference in an $[\text{O III}]$ -selected sample. Table 2 compares the median and distribution widths for the various samples.

4.2. X-ray-loud Composite Galaxies

Thirty X-ray sources have $[\text{O III}]/\text{H}\beta$ ratios and $U - B$ colors that place them in the star-forming area of the emission-line diagnostic diagram. X-rays can be produced in star-forming galaxies by high-mass X-ray binaries, low-mass X-ray binaries, supernova remnants, and hot interstellar medium heated by supernova (Fabbiano 1989) in addition to possible AGNs. Many authors have shown that in starburst galaxies without an AGN, the total X-ray luminosity correlates with the star formation rate (Nandra et al. 2002; Bauer et al. 2002; Ranalli et al. 2003; Grimm et al. 2003; Colbert et al. 2004; Persic et al. 2004; Hornschemeier et al. 2005; Georgakakis et al. 2006; Persic & Rephaeli 2007; Rovilos et al. 2009). Thus the expected X-ray flux from the sources related to SF can be predicted if the SFR is known. We used the Ranalli et al. (2003) calibration to estimate the expected X-ray luminosity from sources related to star formation.

Figure 8 compares observed X-ray luminosities with star formation rates computed from $\text{H}\beta$. Moustakas et al. (2006) provide an empirical calibration to derive SFR from the observed $\text{H}\beta$ strength. The calibration coefficients depend on the rest-frame B -band absolute magnitudes (M_B) of the galaxies. We linearly interpolated between the points given in Table 1 of Moustakas et al. (2006). This is equivalent to applying an average extinction correction in bins of M_B . As shown by Moustakas et al. (2006), when lacking a reliable extinction measurement from $\text{H}\alpha/\text{H}\beta$ ratio, this empirical $\text{H}\beta$ calibration can achieve a SFR estimate good to $\pm 40\%$ (1σ).

Most of the X-ray-loud composite galaxies have X-ray luminosities much higher than star formation can account for in both the soft and hard bands. The excess is more than two orders of magnitude in the extreme cases. A large fraction of the X-ray luminosity in these objects must come from a central AGN. These galaxies therefore appear to be undergoing both star formation and nuclear activity. Since AGN will also contribute to the total $\text{H}\beta$ luminosity, the SFR could be overestimated, which leads to an underestimate of the AGN component.

Further evidence for the coexistence of SF and a central AGN comes from the distribution of the $L_{\text{H}\beta}/L_X(2-10 \text{ keV})$ ratio as a function of the observed X-ray hardness ratio (HR), plotted in Figure 9. X-ray-loud composite galaxies have $L_{\text{H}\beta}/L_X(2-10 \text{ keV})$ ratios higher than typical AGNs but lower than pure star-forming galaxies. Based on the Ranalli et al. (2003) relation between $L_X(2-10 \text{ keV})$ and SFR, and Kennicutt (1998)’s relation between $L_{\text{H}\alpha}$ and SFR, assuming case B Balmer decrement $\text{H}\alpha/\text{H}\beta = 2.85$, typical star-forming galaxies should have $L_{\text{H}\beta}/L_X(2-10 \text{ keV})$ greater than 1 (assuming $A_V \leq 2$). Unambiguous and Type 1 AGNs have an $L_{\text{H}\beta}/L_X(2-10 \text{ keV})$ lower by two orders of magnitude, around 10^{-2} . However, most X-ray-loud composite galaxies have intermediate ratios in $L_{\text{H}\beta}/L_X(2-10 \text{ keV})$. The simplest explanation is that they are composite objects having both star formation and active nuclei. Most of their $\text{H}\beta$ emission originates from star-forming H II regions, while most X-ray emission originates from matter around the SMBH. For example, assuming the intrinsic $L_{\text{H}\beta}/L_X(2-10 \text{ keV})$ ratio for AGNs is 10^{-2} and for pure star-forming galaxies is 10, a galaxy with $\log L_{\text{H}\beta}/L_X(2-10 \text{ keV}) = -1$, in the absence of extinction, 90% of the $\text{H}\beta$ emission comes from star-forming H II regions, and 10% comes from the

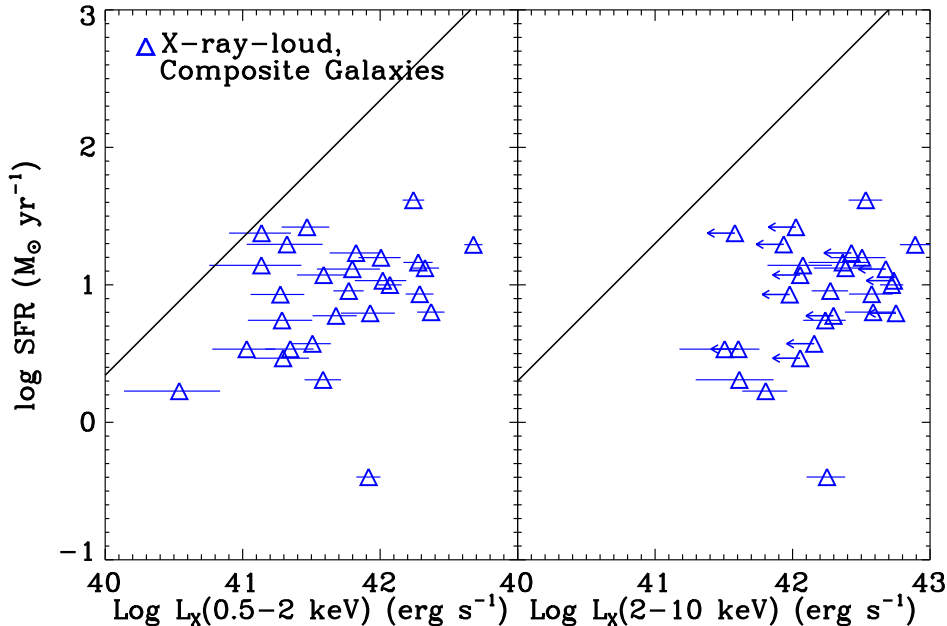


FIG. 8.— SFR derived from $H\beta$ versus the X-ray luminosity for our X-ray-loud composite galaxies—i.e., X-ray sources that appear as star-forming galaxies in emission-line diagnostics. The left panel is for the soft band (0.5–2keV), and the right panel is for the hard band (2–10 keV). The solid lines indicate the SFR– L_X relation calibrated by Ranalli et al. (2003). Median uncertainty in $\log(\text{SFR})$ is 0.20 dex and is dominated by the scatter in the level of extinction among galaxies.

narrow-line region around an AGN. In contrast, 1% of the hard X-ray emission comes from X-ray binaries and supernova remnants, and 99% comes from the AGN. If extinction on $H\beta$ is present at the same level for both the star-forming and nuclear regions, the resulting proportions do not change. Figure 9 shows a relatively clean separation between unambiguous AGNs and X-ray-loud composite galaxies in the $L(H\beta)/L_X$ versus hardness ratio diagram. This supports the hypothesis that our classification scheme is separating objects with different natures.

NGC 6221 provides a local example of a composite object (Levenson et al. 2001) with the X-ray flux dominated by the nucleus and the visible spectrum dominated by the surrounding starburst. As Levenson et al. (2001) showed, besides X-ray, one can detect the AGN component in NGC 6221 by the additional broad component of the [O III] line in a high S/N nuclear spectrum or with high resolution optical or NIR imaging. Our objects are much more luminous than such local examples but otherwise have similar characteristics.

Because the $H\beta$ emission in X-ray-loud composite galaxies is dominated by star-forming H II regions, the SFR derived from it are not too far off: they could be overestimated by $\sim 10\%$. As shown in Figure 8, the inferred star formation rates in these galaxies range from a couple to tens of $M_\odot \text{ yr}^{-1}$ with a median of $10 M_\odot \text{ yr}^{-1}$, typical of $z \sim 1$ star-forming galaxies (Noeske et al. 2007) and similar to the range of SFR found among X-ray selected AGNs at $z \sim 0.8$ (Silverman et al. 2009). The extinction correction applied is only correct on average but not accurate for each individual galaxy. We therefore advise against overinterpreting individual SFR values before better extinction estimates are made.

An alternative explanation for the X-ray-loud composite galaxies might be that these objects are pure AGNs

without star formation, but the X-ray luminosity is heavily absorbed by a large column density of gas. This cannot be the case for two reasons. First, it conflicts with the optical classification. Second, this possibility is not supported by the X-ray hardness ratio as shown in Fig. 9. The hardness ratio is a very rough indicator of the X-ray spectral shape, which relates to the level of absorption. An unabsorbed X-ray spectrum has a low hardness ratio (~ -0.5). Because the opacity is larger for less energetic photons, more absorption generally leads to a harder spectrum and a larger hardness ratio. Though this correlation is loose and is dependent on redshift (Trouille et al. 2009), nonetheless, as shown in Fig. 9, nearly all of our composite galaxies have low hardness ratios, consistent with being unabsorbed.

The lower panel of Figure 9 shows $L(H\beta)/L_X(0.5-2 \text{ keV})$ vs. the hardness ratio. The X-ray-loud composite galaxies still mainly populate a region different from unambiguous AGNs, but the separation between the two classes is not as clean as for the hard band. This is because extinction in the soft band decreases $L_X(0.5-2 \text{ keV})$ as hardness ratio increases, and the overall distribution of points shows an overall counterclockwise rotation.

Figure 9 shows a few X-ray-loud composite galaxies outside their normal region on the plot. At least some of them are likely to be composites of two separate objects rather than a single composite galaxy. This is established for one case, DEEP2 object 12016714,⁵ which has $H\beta/L_X(2-10 \text{ keV})$ even lower than the typical value for unambiguous AGNs. *HST*/ACS imaging reveals that the single object in the DEEP2 CFH12K catalog is in fact two galaxies separated by $1''.5$. The bluer one is brighter

⁵ DEEP2 object number; see <http://deep.berkeley.edu/DR1/photo.primer.html>.

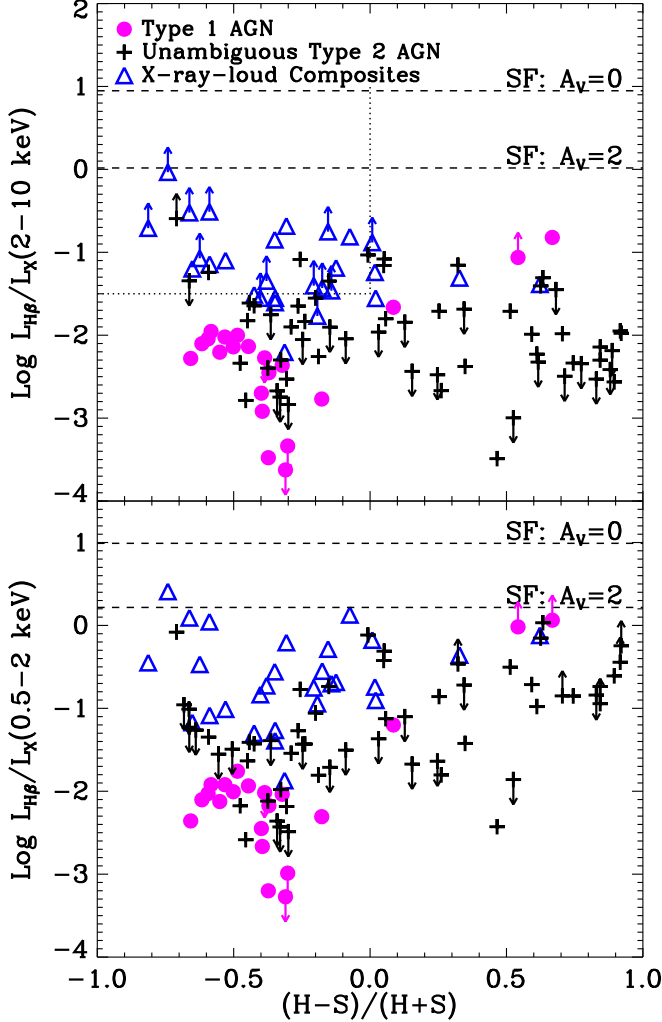


FIG. 9.— Upper: $L_{H\beta}/L_X$ versus hardness ratio for Type 1 AGNs (magenta circles), unambiguous Type 2 AGNs (black crosses), and X-ray-loud composite galaxies (blue triangles). The two horizontal dashed lines mark the expected $L(H\beta)/L_X$ ratios from star-forming galaxies with zero or 2 mag of extinction. The dotted lines indicate a rough demarcation for the boundary between the region occupied by X-ray-loud composite galaxies and typical AGNs. Here $L_{H\beta}$ has not been corrected for extinction. The figure shows all Type 1 AGNs and all unambiguous Type 2 AGNs that are detected in either 2–10 keV band ($p < 0.01$) or $H\beta$. For objects detected in one of these measures, 2–10 keV or $H\beta$ but not both, the corresponding upper or lower limits in the ratio are indicated by the downward or upward arrows, respectively. Lower: same as upper but for the soft band (0.5–2 keV).

in R and thus was targeted by DEEP2. However, the X-ray point source is centered on the other, redder, galaxy. In total, 14 of our 30 X-ray-loud composite galaxies were imaged by *HST*/ACS (Lotz et al. 2008). From visual inspection, two others (DEEP2 12004519, 13049115) out of the 14 are actually close pairs whose components were not separable in the ground-based images, and we cannot tell which component contributed either the spectrum or the X-ray flux. Based on these very rough statistics, we expect 20% of all X-ray-loud composite galaxies in our sample could be unrelated objects that cannot be separated by the limited resolution ($0''.6$ – $1''$ FWHM) of the ground-based images used for photometry.

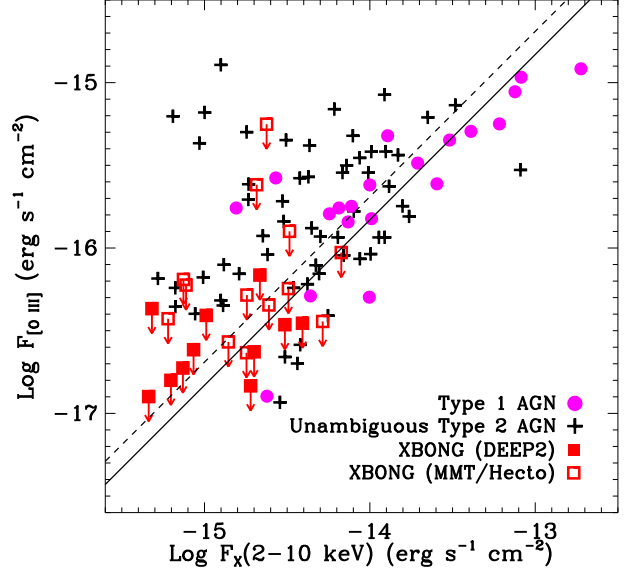


FIG. 10.— $[O\ III]$ line flux (2σ upper limit for non-detections) vs. X-ray flux at 2–10keV for XBONGs (red squares), Type 1 AGNs (magenta circles), and Unambiguous Type 2 AGNs (black crosses). Only sources that are detected ($p < 0.01$) in the hard band are included in this plot. The dashed line indicates the median flux ratio found by Heckman et al. (2005) for Type 1 AGNs, and the solid line indicates the median flux ratio for our Type 1 AGN sample. Those XBONGs with DEEP2 spectra are plotted as solid squares. XBONGs follow the same $[O\ III]$ –X-ray relation as other emission-line AGNs. They do not appear to be a physically distinct population.

4.3. Nature of XBONGs

XBONGs are X-ray sources found in quiescent galaxies for which both $[O\ III]$ and $H\beta$ are undetected ($< 2\sigma$). First, we need to confirm the origin of the X-ray emission. Besides AGNs, X-ray binaries and hot gas in normal galaxies can also produce X-ray emission. Most of the galaxies in this category are red galaxies with early-type morphology. As shown by Fabbiano et al. (1992) and Hornschemeier et al. (2005), the X-ray luminosity in early types has contributions from both X-ray binaries and hot gas, whose total luminosity correlates with the stellar mass ($\log L_X \propto 1.8 \log M_*$). We converted the relation given by Hornschemeier et al. (2005) to our bands assuming a thermal Bremsstrahlung spectrum with $T = 1\text{keV}$ and estimated the expected luminosities for our sources. Only 3 out of the 32 X-ray sources among quiescent galaxies are both consistent with this origin in hardness ratio and have luminosities (in both soft and hard bands) within a factor of 3 of the Hornschemeier et al. (2005) relation. These objects could possibly be normal galaxies without active nuclei. Therefore, we conclude that 29 out of the 32 sources in this category appear to have their X-ray emission dominated by an AGN.

Yuan & Narayan (2004) argued that XBONGs are powered by a radiatively inefficient accretion flow resulting in the lack of emission-line regions and UV/optical bump. Others (Moran et al. 2002; Trump et al. 2009b) have suggested that the narrow line emission in these objects is diluted by the host galaxy, while Rigby et al.

(2006) argued that heavy extinction in the host galaxy is responsible for the lack of optical emission lines. However, none of these analyses has tried to evaluate how much narrow-line emission is expected given the observed X-ray flux and whether the non-detections are beyond expectations. For our sample of XBONGs, we compare their emission line upper limits with their X-ray luminosity to address this problem.

Here, we only use the term XBONG to refer to galaxies without any detectable line emission in the DEEP2 or Hectospec spectra. Previous literature on XBONGs (e.g. Rigby et al. 2006) has included X-ray AGNs that are optically classified as star-forming galaxies. As discussed above, these galaxies do appear to host weak AGNs which are drowned out by the line emission from star-forming HII regions. Because the majority of star-forming galaxies are spiral disk galaxies, they will show a wide range of axis ratios. The inclusion of these X-ray-loud composites in the “optically dull” AGN sample of Rigby et al. (2006) can explain the wide range of axis ratios they found, which were incorrectly used to argue for host extinction effect.

In our analysis, we only focus on those sources without any emission lines, which are sometimes referred to as absorption-dominated, quiescent, or passive galaxies. 6 of our 29 AGN-dominated XBONGs actually have [O II] $\lambda 3727$ significantly ($>2\sigma$) detected. For consistency, we still count them as XBONGs as if [O II] were not covered in the spectra. These objects would likely be classified as LINERs in a standard BPT diagram as they have very high [O II]/ $H\beta$ ratios (Yan et al. 2006).

Figure 10 shows the [O III] flux upper limits vs. hard-X-ray flux distribution for XBONGs in our sample along with more typical AGNs. The [O III]-to-X-ray ratios of the XBONGs are consistent with other AGNs. Their [O III] upper limits are not low enough to indicate that they are significantly weaker in their narrow-line emission relative to their X-ray emission, and they could simply be the tail of the distribution in [O III]-to-X-ray ratio. In fact, many of our XBONGs show weak [O III] emission that is just slightly short of the 2σ detection threshold. The median significance of the [O III] EW measurement (EW divided by its uncertainty) among XBONGs is 1.2; 60% are more than 1σ significant.

The XBONGs in our sample have much lower X-ray fluxes than the typical XBONGs discussed in the literature. All our sources have hard X-ray flux lower than $6.7 \times 10^{-15} \text{erg s}^{-1} \text{cm}^{-2}$, a factor of four lower than the prototype XBONG discussed by Comastri et al. (2002), which has an X-ray flux of $F_{2-10\text{keV}} = 2.5 \times 10^{-14} \text{erg s}^{-1} \text{cm}^{-2}$. A simple explanation for this is that DEEP2 spectra, with their higher than typical spectral resolution and signal-to-noise, are able to probe significantly deeper on [O III] flux amid the stellar light and thus reveal optical AGN signatures for much fainter objects than before. The sample shown here includes both spectra from the DEEP2 survey and spectra taken in the MMT/Hectospec follow-up program. The latter data have lower spectral resolution. If limited to DEEP2-only sources (solid squares in Fig. 10), the XBONGs are even fainter: i.e., objects which would be classified as XBONGs in the Hectospec data yield significant detections if observed by DEIMOS.

Therefore, before we consider any complicated pos-

sibilities to explain XBONGs, we should evaluate the simplest explanation for the non-detection of [O III] in these AGNs: given the observed X-ray flux, the expected [O III] line strength assuming typical AGN flux ratios is simply beyond our detection capability. Our measurements of [O III] upper limits are consistent with this explanation. The [O III]-to-X-ray flux ratios for our XBONGs are consistent with those of other narrow-line AGNs and Type 1 AGNs. They are simply near the tail of the [O III] flux distribution at the corresponding X-ray flux. We do not need to invoke higher than usual host galaxy extinction to explain them, nor any other physical mechanism to suppress the narrow-line strength. If these galaxies have the same [O III]-to-X-ray ratio as Type 1 AGNs, the emission lines would not have been easily detectable in our spectra. Therefore, we see no reason to postulate that they are a different type of object, given the current observations.

If dilution were the main cause for emission lines in these galaxies to be undetected, we would expect that XBONGs should have a brighter rest-frame magnitude in bands bracketing [O III] than those X-ray sources with similar hard-X-ray luminosities. We investigate this by comparing a sample of our XBONGs with a sample of unambiguous AGNs matched in hard-X-ray luminosity. We limit both samples to objects with hard-X-ray (2-10 keV) luminosity between $10^{41.8} \text{erg s}^{-1}$ and $10^{42.8} \text{erg s}^{-1}$. We can then compare their absolute magnitudes in the continuum bands bracketing [O III], which we used to derive the [O III] luminosity in §2.3. It turns out that the two samples have indistinguishable distributions in this magnitude. The median [O III] sideband magnitudes (AB) for the two samples are also very similar: -20.8 for the XBONGs and -20.9 for the unambiguous AGNs. There is no systematic difference between the two samples. In only one object—the XBONG with the highest [O III] flux upper limit—is the host galaxy so bright ($M = -23.25$) that it is conceivable that dilution could be responsible for the non-detection. In most cases, dilution by the host galaxy is not stronger in XBONGs than in other AGN hosts.

If extinction in the host galaxies was the main cause for the emission lines to be undetected, these galaxies would be significantly redder than other AGN hosts and have smaller axis ratios (b/a). We checked this using the above luminosity-matched comparison sample. The median $U - B$ color is 1.14 for the XBONGs and 1.07 for the luminosity-matched unambiguous AGN sample. A Kolmogorov-Smirnov test on the two distributions indicates that the probability of obtaining the observed difference, given the null hypothesis that the two samples are drawn from the same parent distribution, is 37%, meaning the difference is not statistically significant. To produce such a difference by extinction only requires an A_V of 0.33 magnitude (assuming $R_V = 3.1$), which will only dim the [O III] emission lines by 30% or 0.15 dex. Therefore, extinction cannot be the primary reason for the nondetection of emission lines. Additionally, 11 out of the 29 AGN-dominated XBONGs were imaged with *HST*/ACS. The smallest axis ratio found among them is 0.37 in the $F814W$ band. Their axis ratio distribution is indistinguishable from that of the unambiguous Type 2 AGNs, as shown in Fig. 11.

The fraction of XBONGs in our sample at $0.3 < z <$

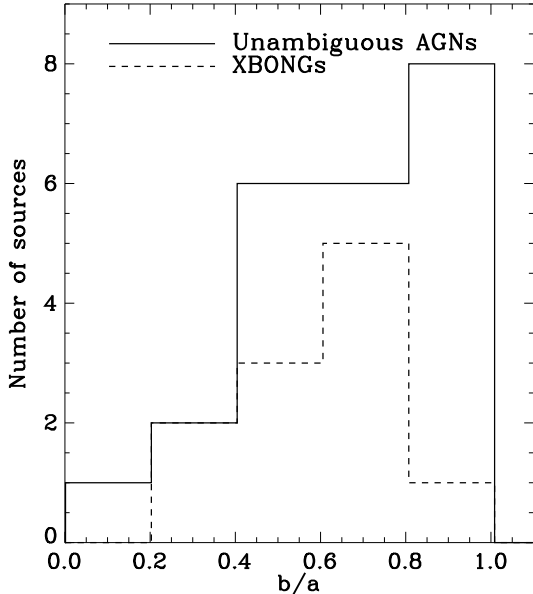


FIG. 11.— Axis ratio distributions for unambiguous AGNs (solid histogram) and XBONGs (dashed histogram). Only sources imaged with *HST*/ACS are included. The two distributions are indistinguishable statistically, suggesting that extinction by host galaxies is not the primary cause for the nondetection of emission lines in XBONGs.

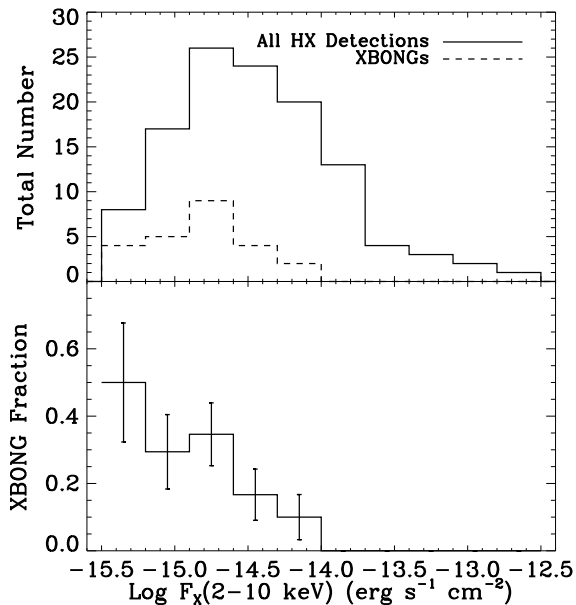


FIG. 12.— Top: the distribution of the 2–10 keV flux for all XBONGs (dashed line histogram) detected ($p < 0.01$) in the hard X-ray band compared to the flux distribution for all hard-X-ray-detected sources (solid line histogram). Bottom: the fraction of XBONGs as a function of hard X-ray flux. The fraction decreases with increasing flux, which suggests that the non-detections are due to the faint X-ray flux of the AGNs.

0.8 is smaller than previously reported in the literature in the same redshift range ($\sim 30\%$ in Trump et al. 2009a if limited to $0.3 < z < 0.8$) and depends strongly on X-ray flux. Among all 146 spectroscopically identified X-ray sources that have both [O III] and $H\beta$ well covered in the spectra, we have 32 XBONGs, 29 of which are definitely AGNs. This is $19.9\% \pm 3.3\%$. If we limit to DEEP2 spectra only, which have better quality, the fraction is slightly lower, $14.7\% \pm 3.5\%$ (15 out of 102 sources). Figure 12 shows the fraction of XBONGs as a function of hard X-ray flux, among sources that have a measurable hard X-ray flux. The fraction decreases strongly toward higher X-ray flux. This is consistent with the simple explanation above that XBONGs are purely the result of observational limitations rather than comprising a physically distinct class of AGNs.

We thus find no evidence suggesting that those X-ray sources with no detected emission-lines must be a separate population from other emission-line AGNs; neither greater dilution nor higher than usual host galaxy extinction appears consistent with our observations. To rule out the null hypothesis that they are the same as other emission-line AGNs, we need to obtain much higher quality spectra. Until the time we detect their emission lines and find their emission-line-to-X-ray ratio is distinctively lower than other AGNs, or until we push the emission-line upper limits to a correspondingly low level, there is no reason to classify them separately. Collecting high-quality spectroscopic data is the best way forward.

4.4. Incompleteness of the Optical AGN Selection

The combination of the three classes of objects discussed above comprises the whole sample of objects that are detected in ~ 200 ks *Chandra* exposures, spectroscopically identified, brighter than I_{AB} of 22, and have redshifts between $0.3 < z < 0.8$. Most of these objects, regardless of their X-ray luminosity, host an AGN. When classified with optical emission-line diagnostics, they fall into three classes: emission-line AGNs, star-forming galaxies, and quiescent galaxies. This reveals the weakness of optical classification when compared with X-ray selection. Optical AGN selection not only selects on the bolometric luminosity of the AGN, it also selects on other properties of the host galaxy, primarily star formation rate. In the absence of extinction affecting emission lines and absorption of X-rays, a narrow-line AGN with a 2–10 keV luminosity of $1.7 \times 10^{42} \text{ erg s}^{-1}$ can be easily drowned out in emission line luminosity by an SFR of $10 M_{\odot} \text{ yr}^{-1}$, a case in which 97% of the $H\beta$ emission comes from star-forming HII regions, but 97% of the hard X-ray flux comes from the AGN.

Most XBONGs should not be counted toward the incompleteness of the optical AGN selection, because the intrinsic bolometric luminosity of these AGNs is simply beyond the detection limit of the optical selection. However, the emission line detection limit in the optical spectra is not simple to estimate. The detectability depends on many factors: the line flux, the stellar continuum flux, the sky background flux, and the complexity of the stellar continuum modeling. It also depends on many parameters of the observations, such as the exposure time and the seeing at the time of observation, which could vary even in the same survey.

Optical selection is also sensitive to extinction, which

we have not discussed in detail. For AGN narrow-line regions, it is usually not a severe concern except in edge-on disk galaxies. The median extinction on [O III] among typical Type-2 Seyferts is around 1.0 mag (LaMassa et al. 2009; Diamond-Stanic et al. 2009). Extinction can be corrected for when attenuation measurements are available, or one can exclude edge-on disk galaxies from the analysis.

Perhaps the most fundamental weakness of optical diagnostics is its dependence on high quality spectra, which becomes increasingly expensive to obtain for fainter galaxies. Many X-ray sources have very faint optical counterparts or no counterparts. In our investigation, we only considered objects with $I_{AB} < 22$ for completeness and signal-to-noise reasons. In fact, based on photometric redshifts obtained from the CFHT Legacy Survey (Ilbert et al. 2006), about 40% of X-ray sources with an optical counterpart in CFHTLS and with $0.3 < z_{\text{phot}} < 0.8$ have $I_{AB} > 22$. Compared to our sample, most of them are probably less massive galaxies, which have less massive black holes. The AGN demographics of these sources could also be different. We leave this for future investigations.

4.5. *Optical-only AGNs and the Incompleteness of the X-ray selection*

Of the objects which are identified as AGNs from their emission line ratios but lacking X-ray detections, all but one are Type 2 AGNs. Figure 13 plots the upper limits for the 2–10 keV flux and luminosity for these sources along with the unambiguous AGNs. Most of the optical-only AGNs lie to the upper left of the Heckman et al. (2005) relation, i.e., they have much lower $L_X(2-10 \text{ keV})/L_{[\text{O III}]}$ ratios. This is consistent with the conclusions of Heckman et al. (2005) based on local AGN samples: optically selected samples have much lower median $L_X(2-10 \text{ keV})/L_{[\text{O III}]}$ ratio than X-ray selected samples and have broader distributions in flux ratio. This indicates that optically selected samples include more heavily absorbed sources and possibly Compton-thick sources, which are missed by X-ray selection techniques. Therefore, an AGN sample selected based on a hard-X-ray luminosity threshold in 2–10 keV will not be a complete bolometric-luminosity-limited sample due to cases of heavy absorption and Compton-scattering of X-ray photons.

Another potential explanation for the high [O III]-to-X-ray ratio of these objects is that they have star formation contributing significantly to the [O III] flux but not the X-ray. This cannot be the case for two reasons. First, these galaxies are classified as AGNs according to their emission-line ratios indicating that their [O III] flux must be dominated by an AGN. Second, star formation would make these galaxies appear bluer than other AGNs. The $U - B$ color distribution for optical-only AGNs is statistically indistinguishable from that of the unambiguous Type 2 AGNs. Therefore, the high [O III]-to-X-ray ratios of optical-only AGNs cannot be due to contamination by star formation.

One might worry that these optical-only AGNs are dusty star-forming galaxies. For most of them, this cannot be the case. The stellar mass distribution of these optical-only AGNs is statistically indistinguishable

from those AGNs detected in the X-ray (the unambiguous AGNs). On the other hand, they are much more massive than those star-forming galaxies with the same [O III]/ $H\beta$ ratios. The latter has a median stellar mass of $10^{9.9} M_{\odot}$, which is only one-tenth of the median mass of optical-only AGNs, $10^{11.0} M_{\odot}$. The difference is much larger than their respective standard deviations, a factor of 2.8 for the star-forming galaxies and a factor of 2.3 for the optical-only AGNs. The two drastically different stellar mass distributions demonstrate that the majority of optical-only AGNs cannot be dusty star-forming galaxies.

Some may also argue that our emission-line selection includes both Seyferts and LINERs (Low-ionization nuclear emission-line regions), and some fraction of LINERs could be powered by processes unrelated to accretion onto SMBHs (Binette et al. 1994; Sarzi et al. 2010). The recent study by Sarzi et al. (2010) using data from the SAURON survey showed that ionization processes other than AGN photoionization can contribute up to 2Å of [O III] EW with LINER-like [O III]/ $H\beta$ ratios in integrated spectra taken with an SDSS fiber aperture. Many (35%, 101 out of 291) of our emission-line-selected AGNs have [O III]/ $H\beta$ (or lower limits) greater than 3, satisfying the traditional definition for Seyferts (Ho et al. 1997). 35% (67 out of 190) of the remaining objects in our emission-line AGN sample, which we call LINERs, have [O III] EWs greater than 3Å, thus definitely having substantial AGN contribution. In fact, 13% of those LINERs with [O III] EW less than 3Å in our sample are also detected at X-ray wavelengths, suggesting many of them are indeed AGNs, rather than powered by shocks or old stellar populations.

To evaluate what fraction of genuine AGNs are not detected in the hard X-ray due to the absorption of the X-ray emission, we need to take into account the variable sensitivity limit across each *Chandra* pointing. Thus, we first estimate how many of the optically selected AGNs would be detectable in the observed 2–7 keV band if they were not absorbed, and then compare this with the actual number of 2–7 keV detections. We limit this calculation to the DEEP2 optical-AGN sample because the Hectospec observation gave priorities to X-ray sources in target selection. We also exclude weak LINER sources with [O III]/ $H\beta < 3$ and $\text{EW}([\text{O III}]) < 3\text{Å}$ to limit contamination from sources not photoionized by an AGN. This is a very conservative AGN sample. Including both Type 1 and Type 2 optical AGNs, we have a sample of 140 objects. Our results do not change at all if we strictly limit to only Seyferts, i.e., excluding all the LINERs regardless of [O III] EW.

Assuming the observed [O III] fluxes reflect the intrinsic luminosities of the AGNs, we estimated the unabsorbed hard-X-ray fluxes for all optical AGNs using the median hard-X-ray-to-[O III] ratio of Type 1 AGNs in our sample, which is 1.83 dex. Given the X-ray exposure map, the background map, and the redshift of each source, assuming an unabsorbed power-law spectrum with a photon index of $\Gamma = 1.9$, we converted the flux of each source to the expected source counts in the 2–7 keV band. We then calculated, for each source, the probability of observing enough counts to qualify it as an X-ray detection in the hard band, given the background counts at the position. The sum of these probabilities

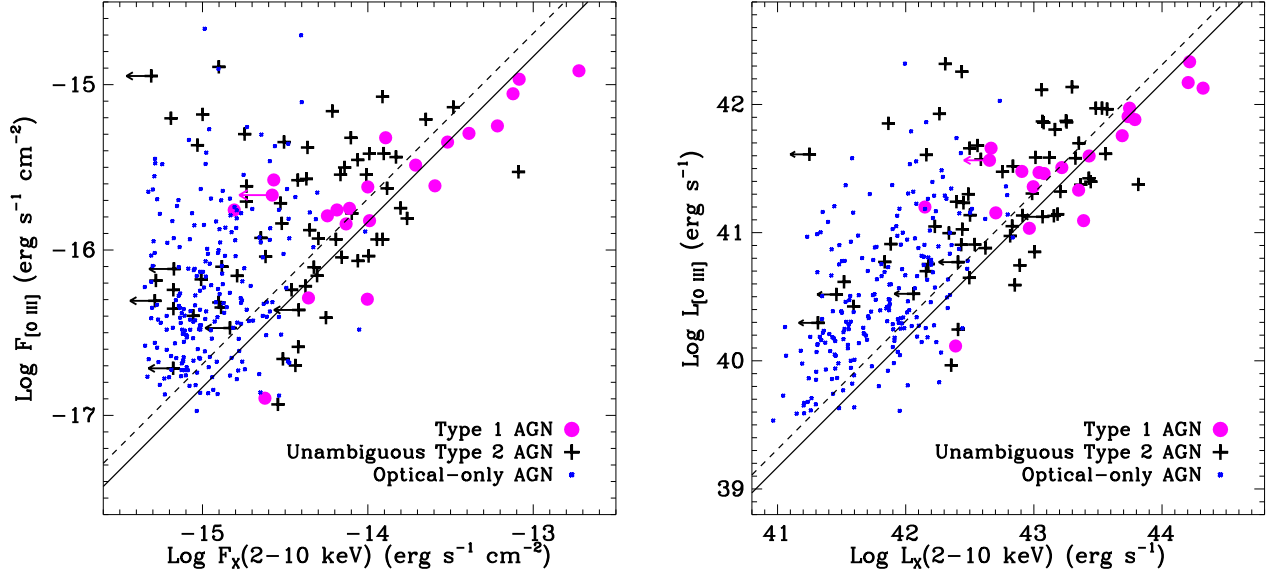


FIG. 13.— Left: $[\text{O III}]$ line flux vs. X-ray flux in 2–10 keV for Type 1 AGNs (magenta circles), unambiguous Type 2 AGNs (black crosses), and optical-only AGNs (small blue dots); the combination of these subsamples forms the optically selected AGN population. Optical-only AGNs are undetected in the hard X-ray, thus their upper limits are shown without arrows for clarity. The dashed line indicates the median flux ratio found by Heckman et al. (2005) for Type 1 AGNs. The solid line indicates the median flux ratio for our Type 1 sample. As seen here, Type 2 AGNs have a broader distribution in $[\text{O III}]/\text{X-ray}$ ratio and mostly have lower hard-X-ray-to- $[\text{O III}]$ ratios than Type 1 AGNs. Right: Similar to the left panel but comparing luminosity rather than flux.

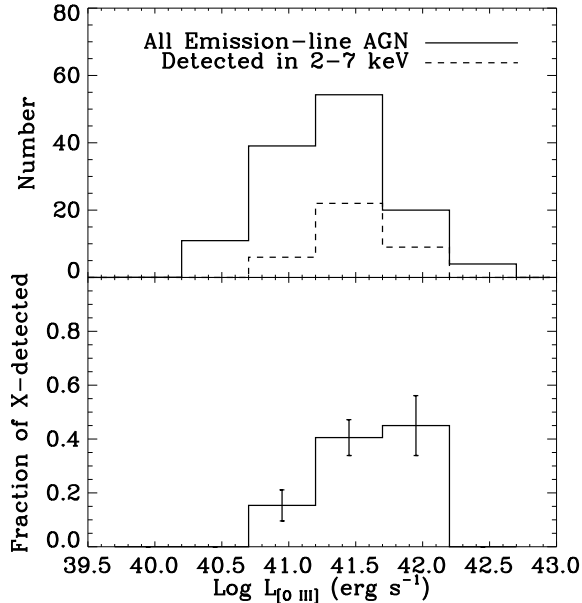


FIG. 14.— Top: the solid histogram shows, in each $[\text{O III}]$ luminosity bin, the sum of the 2–7 keV band detection probabilities of all optically selected AGNs (including Type 1s) assuming their X-rays were not absorbed. Only DEEP2 objects are included. LINERs (objects satisfying the AGN cuts shown in Fig. 6 and having $[\text{O III}]/\text{H}\beta < 3$) with $[\text{O III}]$ EW less than 3\AA are excluded to limit contaminations. The dashed histogram shows the number of actual 2–7 keV detections ($p_{2-7 \text{ keV}} < 4 \times 10^{-6}$) in each $[\text{O III}]$ luminosity bin. Bottom: fraction of 2–7 keV detections among optically-selected AGNs as a function of $[\text{O III}]$ luminosity.

is the total number of detectable AGNs if their X-rays were not absorbed at all. Dividing the number of actual hard-X-ray detections by the sum of the probabilities yields the X-ray detection fraction, i.e., the fraction of actual detections out of all potentially X-ray detectable AGNs if the X-rays were not absorbed. For the 140 objects in the sample defined above, the sum of their hard band detection probabilities is 128.31. In reality, only 37 sources (29%) are detected in the hard band. If we limit to Seyferts only ($[\text{O III}]/\text{H}\beta > 3$), the fraction is the same: out of 91 Seyferts in our sample, the sum of their potential 2–7 keV detection probability is 88.42; while only 26 sources (29%) are actually detected.

The X-ray detection fraction in bins of $[\text{O III}]$ luminosity is plotted in Figure 14. The fraction of hard X-ray detection among all potentially-detectable AGNs decreases toward lower $[\text{O III}]$ luminosity. At the bright end, $\sim 50\%$ of all AGNs are detected in the 2–7 keV band, which includes unabsorbed and moderately absorbed AGNs. At the faint end, the detection rate rolls off because more and more moderately absorbed AGNs fall below the detection threshold.

This demonstrates the weakness of X-ray selection relative to optical selection. Depending on the survey depth, X-ray selection can miss a substantial population of AGNs due to absorption and, in some cases, Compton scattering of X-rays by clouds exterior to the accretion disk but interior to the narrow-line region. At $L_{[\text{O III}]} > 10^{40.5} \text{ erg s}^{-1}$, the overall hard X-ray detection fraction is $29.5\% \pm 4.1\%$. Assuming an $[\text{O III}]$ bolometric correction of 3500 (Heckman et al. 2004), this corresponds to $L_{\text{bol}} > 1.1 \times 10^{44} \text{ erg s}^{-1}$ or intrinsic, unabsorbed $L_X(2-10 \text{ keV}) > 2.1 \times 10^{42} \text{ erg s}^{-1}$ if the median flux ratio of Type 1 AGNs is applied. Above this

threshold in intrinsic luminosity, 70% of all potentially detectable AGNs would not be detected (at $p < 4 \times 10^{-6}$) in the 2–7 keV band in 200 ks *Chandra* images due to X-ray absorption and/or scattering.

4.6. Column density distribution at high- z

Using our emission-line selected AGN sample, we can evaluate whether the absorbing column density distribution among high- z AGNs is different from that in the local universe. Following most local studies, we focus on Seyfert 2 galaxies only. As shown by Bassani et al. (1999), the column density corresponds closely to the $\text{HX}/[\text{O III}]$ ratio. By applying the observed hard-X-ray-to- $[\text{O III}]$ -ratio distribution of a local sample of Seyfert 2s to our high- z sample, we can simulate the expected detection fraction of high- z Seyferts if the column density distribution among Seyfert 2s does not evolve with redshift.

For the local Seyfert 2 sample, we employed the $[\text{O III}]$ -selected sample collected by Heckman et al. (2005). They provide the observed $\text{HX}/[\text{O III}]$ ratios without any correction for extinction of $[\text{O III}]$ or absorption of X-ray, which is ideal for our purpose. There are 32 Seyfert 2s in this sample, 29 of which have 2–10 keV X-ray data available. We combined ratios randomly drawn from this local sample with the observed $[\text{O III}]$ fluxes of our high- z Seyfert 2s to predict their rest-frame 2–10 keV luminosities. With inverse K -correction and conversion from flux to counts (both assuming $\Gamma = 1.9$), we predicted the observed 2–7 keV counts distribution and the total detection fraction. The effect of Γ in inverse K -correction and the flux-to-counts conversion largely cancel out. Assuming the unabsorbed spectral index will lead to a slight underestimate⁶ of the observed counts and a lower limit on the detection fraction. With 5000 simulations, we find the expected 2–7 keV detection ($p < 4 \times 10^{-6}$) fraction has a mean of 39% and a dispersion of 5%. In reality, only $25\% \pm 5\%$ of our Seyfert 2s are detected in the 2–7 keV band, which is 2σ smaller than expected if the column density distribution does not evolve with redshift. This suggests that an average Seyfert 2 galaxy between redshift 0.3 and 0.8 has at least the same, or marginally higher, column density than the average local Seyfert 2 galaxy.

We also ran simulations with different detection thresholds to see whether the increased detection fraction of Seyferts will lead to different conclusions. The results are listed in Table 3. For the two more relaxed detection thresholds, the differences between the actual detection fraction and the expected detection fraction are smaller and less significant ($\sim 1.3\sigma$). Therefore, we conservatively conclude that, at the current statistical significance, the column density distribution among Seyferts at higher- z is similar to that in the local universe, which suggests the fraction of Compton-thick AGNs are also similar to that in the local universe ($\sim 50\%$; Bassani et al. 1999, Risaliti et al. 1999).

5. SUMMARY AND CONCLUSIONS

This paper has developed a new AGN/SF diagnostic diagram using $[\text{O III}]/\text{H}\beta$ ratio and the rest-frame $U - B$

⁶ If true $\Gamma = 0$, we will underestimate the observed counts at $z = 0.6$ by 18%.

TABLE 3
COMPARISON BETWEEN ACTUAL X-RAY DETECTION FRACTION OF SEYFERT 2S AND SIMULATIONS

Detection Threshold	Detection Fraction	Simulated Fraction
$p < 4 \times 10^{-6}$	$25\% \pm 5\%$	$39\% \pm 5\%$
$p < 1 \times 10^{-3}$	$37\% \pm 5\%$	$46\% \pm 5\%$
$p < 1 \times 10^{-2}$	$43\% \pm 5\%$	$52\% \pm 5\%$

color (in AB system) of the host galaxy. It can be applied to higher redshifts than more traditional line ratio diagnostics as it does not require the use of the $[\text{N II}]/\text{H}\alpha$ ratio. Using both galaxies at $z \sim 0.1$ from the SDSS and galaxies at $0.2 < z < 0.4$ from the DEEP2 survey, we have demonstrated that this diagnostic technique is highly effective for galaxies above the Kewley curve in the traditional BPT diagram; but less effective for galaxies inbetween the Kauffmann and Kewley demarcations. All diagrams share the same weaknesses, when compared with the X-ray selection.

Applying the new diagram to higher redshifts in the AEGIS survey, we classified galaxies into AGNs, star-forming galaxies, and quiescent galaxies. Our sample was selected to have both $[\text{O III}]$ and $\text{H}\beta$ well covered in the spectra, which roughly corresponds to the redshift range $0.3 < z < 0.8$. We selected only sources with $I_{\text{AB}} < 22$ that have secure redshifts, resulting in 3150 objects. Using this sample to compare the optical classification to the X-ray data, we have reached the following conclusions.

1. $57.5\% \pm 4.1\%$ (84 out of 146) of X-ray sources in our sample are also emission-line AGNs according to optical selection techniques, including both Type 1 and Type 2 objects; $19.2\% \pm 3.3\%$ (28/146) of X-ray sources are classified as star-forming galaxies according to our emission-line classification, while $21.9\% \pm 3.4\%$ (32/146) are found to have neither $[\text{O III}]$ nor $\text{H}\beta$ detectable, corresponding to X-ray bright, optically normal galaxies (XBONGs).
2. For those X-ray sources where the optical emission-line ratios indicate star formation, most have X-ray luminosities far exceeding the expectations for pure star-forming galaxies. The simplest explanation is that they have both an AGN and ongoing star formation. Because the $\text{H}\beta$ -to-X-ray ratio in pure star-forming galaxies is 3 orders of magnitude higher than the ratios found in pure AGNs, the emission lines in these galaxies are dominated by SF, and the X-ray emission is mainly powered by an AGN. Combining this emission-line-to-X-ray ratio with the hardness ratio allows us to exclude the possibility of heavily obscured AGNs and to disentangle the contributions from AGNs and star formation.
3. In our sample, 21.9% of X-ray-detected galaxies are found to lack both $[\text{O III}]$ and $\text{H}\beta$ emission lines, which would cause them to be classified as XBONGs. All but 3 of them have X-ray luminosities exceeding the expectations for normal early-type galaxies, indicating the presence of AGNs.

These sources have [O III] upper limits consistent with the expectation from the X-ray luminosity for typical AGNs, i.e., they are not distinctively lower in their [O III]-to-X-ray ratios. There is no reason to assume that XBONGs are a physically different population from other X-ray AGNs. Neither host galaxy dilution nor unusual extinction is primarily responsible for the non-detection of line emission in most of the XBONGs.

4. Our new emission line ratio diagnostics identifies 291 AGNs in our sample, of which 22% are also detected in the X-ray sample. Absorption of the X-rays by gas near the SMBH is necessary to account for most of the non-detections. Taking into account the variable sensitivity across *Chandra* pointings, we estimated the X-ray detection fraction as a function of the observed [O III] luminosity. At $L_{\text{bol}} > 10^{44} \text{ erg s}^{-1}$, about 2/3 of the emission-line AGNs with $0.3 < z < 0.8$ and $I_{\text{AB}} < 22$ will not be detected in the 2–7 keV band in our ~ 200 ks *Chandra* images due to absorption and/or scattering of the X-rays.
5. If the column density distribution of Seyfert 2 galaxies at high z were the same as in the local universe, we would expect a slightly higher fraction of our Seyfert 2s to be detected in the 2–7 keV band than observed. This suggests that Seyfert 2 galaxies at $0.3 < z < 0.8$ have the same or marginally higher average column density than local Seyfert 2s. Thus, we expect the Compton-thick fractions at both redshifts to be similar as well.

Neither optical classification nor X-ray selection yields a complete AGN sample; in fact, both are far from that goal. In the X-ray, heavy absorption by gas in close proximity to the AGN can prevent the detection of a substantial population of AGNs. The optical selection is less affected by obscuring material as the narrow emission lines arise from much larger scales. However, emission lines can easily be drowned out by star formation. Additionally, the detection of line emission requires high quality spectra to subtract the host galaxy stellar light. The combination of the two methods gives a more complete sample. However, heavily X-ray-absorbed AGNs that reside in star-forming galaxies will still be missed. Infrared observations could be the solution to finding AGNs in these cases (Lacy et al. 2004; Stern et al. 2005; Park et al. 2010).

This paper is based on observations taken at the W. M. Keck Observatory which is operated jointly by the University of California and the California Institute of Technology, and the MMT Observatory, a joint facility of the Smithsonian Institution and the University of Arizona.

We thank the anonymous referee who helped us to improve the paper significantly. We thank Greg Wirth and all of the Keck Observatory staff for their help in the acquisition of the DEEP2 Keck/DEIMOS data. We also wish to recognize and acknowledge the highly significant cultural role and reverence that the summit of Mauna Kea has always had within the indigenous Hawaiian community. It is a privilege to be given the opportunity to conduct observations from this mountain.

This study makes use of data from AEGIS, a multiwavelength sky survey conducted with the *Chandra*, GALEX, Hubble, Keck, CFHT, MMT, Subaru, Palomar, *Spitzer*, VLA, and other telescopes and supported in part by the NSF, NASA, and the STFC. The AEGIS website is <http://aegis.ucolick.org>. The DEEP2 website is <http://deep.berkeley.edu/>.

The project was supported in part by the NSF Grants AST00-71198, AST00-71048, AST05-07483, AST05-07428, AST08-07630, AST08-08133, and NASA Chandra grants G05-6141A and GO8-9129A. This research made use of the NASA Astrophysics Data System, and employed open-source software written and maintained by David Schlegel, Douglas Finkbeiner, and others.

Funding for the Sloan Digital Sky Survey (SDSS) has been provided by the Alfred P. Sloan Foundation, the Participating Institutions, the National Aeronautics and Space Administration, the National Science Foundation, the U.S. Department of Energy, the Japanese Monbukagakusho, and the Max Planck Society. The SDSS Web site is <http://www.sdss.org/>. The SDSS is managed by the Astrophysical Research Consortium (ARC) for the Participating Institutions. The Participating Institutions are The University of Chicago, Fermilab, the Institute for Advanced Study, the Japan Participation Group, The Johns Hopkins University, Los Alamos National Laboratory, the Max-Planck-Institute for Astronomy (MPIA), the Max-Planck-Institute for Astrophysics (MPA), New Mexico State University, the University of Pittsburgh, Princeton University, the United States Naval Observatory, and the University of Washington.

Facilities: Keck:II (DEIMOS), MMT (Hectospec), CXO (ACIS), CFHT (CFH12K), HST (ACS)

REFERENCES

- Adelman-McCarthy, J. K., et al. 2008, *ApJS*, 175, 297
 Baldwin, J. A., Phillips, M. M., & Terlevich, R. 1981, *PASP*, 93, 5
 Balogh, M. L., Morris, S. L., Yee, H. K. C., Carlberg, R. G., & Ellingson, E. 1999, *ApJ*, 527, 54
 Barger, A. J., Cowie, L. L., Mushotzky, R. F., & Richards, E. A. 2001, *AJ*, 121, 662
 Bassani, L., Dadina, M., Maiolino, R., Salvati, M., Risaliti, G., della Ceca, R., Matt, G., & Zamorani, G. 1999, *ApJS*, 121, 473
 Bauer, F. E., Alexander, D. M., Brandt, W. N., Hornschemeier, A. E., Vignali, C., Garmire, G. P., & Schneider, D. P. 2002, *AJ*, 124, 2351
 Beers, T. C., Flynn, K., & Gebhardt, K. 1990, *AJ*, 100, 32
 Bell, E. F., McIntosh, D. H., Katz, N., & Weinberg, M. D. 2003, *ApJS*, 149, 289
 Binette, L., Magris, C. G., Stasinska, G., & Bruzual, A. G. 1994, *A&A*, 292, 13
 Blanton, M. R. 2006, *ApJ*, 648, 268
 Blanton, M. R., & Roweis, S. 2007, *AJ*, 133, 734
 Brusa, M., et al. 2003, *A&A*, 409, 65
 Bruzual, G., & Charlot, S. 2003, *MNRAS*, 344, 1000
 Bundy, K., et al. 2006, *ApJ*, 651, 120
 Caccianiga, A., Severgnini, P., Della Ceca, R., Maccacaro, T., Carrera, F. J., & Page, M. J. 2007, *A&A*, 470, 557
 Civano, F., et al. 2007, *A&A*, 476, 1223
 Cocchia, F., et al. 2007, *A&A*, 466, 31
 Coil, A. L., Newman, J. A., Kaiser, N., Davis, M., Ma, C.-P., Kocevski, D. D., & Koo, D. C. 2004, *ApJ*, 617, 765
 Coil, A. L., et al. 2009, *ApJ*, 701, 1484
 Colbert, E. J. M., Heckman, T. M., Ptak, A. F., Strickland, D. K., & Weaver, K. A. 2004, *ApJ*, 602, 231
 Comastri, A., et al. 2002, *ApJ*, 571, 771
 Cooper, M. C., et al. 2008, *MNRAS*, 383, 1058
 Daddi, E., et al. 2007, *ApJ*, 670, 173

- Davis, M., et al. 2003, in *Discoveries and Research Prospects from 6- to 10-Meter-Class Telescopes II*. Edited by Guhathakurta, Puragra. Proceedings of the SPIE, Volume 4834, pp. 161-172 (2003), ed. P. Guhathakurta, 161-172
- Davis, M., et al. 2007, *ApJ*, 660, L1
- Diamond-Stanic, A. M., Rieke, G. H., & Rigby, J. R. 2009, *ApJ*, 698, 623
- Donley, J. L., Rieke, G. H., Pérez-González, P. G., & Barro, G. 2008, *ApJ*, 687, 111
- Elvis, M., Schreier, E. J., Tonry, J., Davis, M., & Huchra, J. P. 1981, *ApJ*, 246, 20
- Elvis, M., et al. 1994, *ApJS*, 95, 1
- . 2009, *ApJS*, 184, 158
- Fabbiano, G. 1989, *ARA&A*, 27, 87
- Fabbiano, G., Kim, D., & Trinchieri, G. 1992, *ApJS*, 80, 531
- Ferrarese, L., & Merritt, D. 2000, *ApJ*, 539, L9
- Fiore, F., et al. 2000, *New Astronomy*, 5, 143
- . 2008, *ApJ*, 672, 94
- Gebhardt, K., et al. 2000, *ApJ*, 539, L13
- Georgakakis, A., Rowan-Robinson, M., Nandra, K., Digby-North, J., Pérez-González, P. G., & Barro, G. 2010, *MNRAS*, 406, 420
- Georgakakis, A. E., Chavushyan, V., Plionis, M., Georgantopoulos, I., Koulouridis, E., Leonidaki, I., & Mercado, A. 2006, *MNRAS*, 367, 1017
- Georgantopoulos, I., Akylas, A., Georgakakis, A., & Rowan-Robinson, M. 2009, *A&A*, 507, 747
- Gilli, R., Comastri, A., & Hasinger, G. 2007, *A&A*, 463, 79
- Grimm, H.-J., Gilfanov, M., & Sunyaev, R. 2003, *MNRAS*, 339, 793
- Groves, B. A., Dopita, M. A., & Sutherland, R. S. 2004, *ApJS*, 153, 75
- Heckman, T. M., Kauffmann, G., Brinchmann, J., Charlot, S., Tremonti, C., & White, S. D. M. 2004, *ApJ*, 613, 109
- Heckman, T. M., Ptak, A., Hornschemeier, A., & Kauffmann, G. 2005, *ApJ*, 634, 161
- Helene, O. 1984, *Nuclear Instruments and Methods in Physics Research A*, 228, 120
- Ho, L. C., Filippenko, A. V., & Sargent, W. L. 1995, *ApJS*, 98, 477
- Ho, L. C., Filippenko, A. V., & Sargent, W. L. W. 1997, *ApJS*, 112, 315
- Hornschemeier, A. E., Heckman, T. M., Ptak, A. F., Tremonti, C. A., & Colbert, E. J. M. 2005, *AJ*, 129, 86
- Ilbert, O., et al. 2006, *A&A*, 457, 841
- Jahnke, K., Kuhlbrodt, B., & Wisotzki, L. 2004, *MNRAS*, 352, 399
- Kauffmann, G., et al. 2003, *MNRAS*, 346, 1055
- . 2007, *ApJS*, 173, 357
- Kennicutt, R. C. 1998, *ARA&A*, 36, 189
- Kewley, L. J., Dopita, M. A., Sutherland, R. S., Heisler, C. A., & Trevena, J. 2001, *ApJ*, 556, 121
- Kraft, R. P., Burrows, D. N., & Nousek, J. A. 1991, *ApJ*, 374, 344
- Lacy, M., et al. 2004, *ApJS*, 154, 166
- Laird, E. S., et al. 2009, *ApJS*, 180, 102
- Lamareille, F. 2010, *A&A*, 509, A53+
- Lamareille, F., Mouhcine, M., Contini, T., Lewis, I., & Maddox, S. 2004, *MNRAS*, 350, 396
- LaMassa, S. M., Heckman, T. M., Ptak, A., Hornschemeier, A., Martins, L., Sontenrucker, P., & Tremonti, C. 2009, *ApJ*, 705, 568
- Levenson, N. A., Cid Fernandes, Jr., R., Weaver, K. A., Heckman, T. M., & Storch-Bergmann, T. 2001, *ApJ*, 557, 54
- Lin, L., et al. 2007, *ApJ*, 660, L51
- Lotz, J. M., et al. 2008, *ApJ*, 672, 177
- Magorrian, J., et al. 1998, *AJ*, 115, 2285
- Maiolino, R., Salvati, M., Bassani, L., Dadina, M., della Ceca, R., Matt, G., Risaliti, G., & Zamorani, G. 1998, *A&A*, 338, 781
- Maiolino, R., et al. 2003, *MNRAS*, 344, L59
- McLure, R. J., Jarvis, M. J., Targett, T. A., Dunlop, J. S., & Best, P. N. 2006, *MNRAS*, 368, 1395
- Moran, E. C., Filippenko, A. V., & Chornock, R. 2002, *ApJ*, 579, L71
- Moran, E. C., Halpern, J. P., & Helfand, D. J. 1996, *ApJS*, 106, 341
- Moustakas, J., Kennicutt, Jr., R. C., & Tremonti, C. A. 2006, *ApJ*, 642, 775
- Mulchaey, J. S., Koratkar, A., Ward, M. J., Wilson, A. S., Whittle, M., Antonucci, R. R. J., Kinney, A. L., & Hurt, T. 1994, *ApJ*, 436, 586
- Mushotzky, R. F., Cowie, L. L., Barger, A. J., & Arnaud, K. A. 2000, *Nature*, 404, 459
- Nandra, K., George, I. M., Mushotzky, R. F., Turner, T. J., & Yaqoob, T. 1997, *ApJ*, 477, 602
- Nandra, K., Mushotzky, R. F., Arnaud, K., Steidel, C. C., Adelberger, K. L., Gardner, J. P., Teplitz, H. I., & Windhorst, R. A. 2002, *ApJ*, 576, 625
- Nandra, K., & Pounds, K. A. 1994, *MNRAS*, 268, 405
- Nandra, K., et al. 2005, *MNRAS*, 356, 568
- Noeske, K. G., et al. 2007, *ApJ*, 660, L43
- Park, S. Q., et al. 2010, *ApJ*, 717, 1181
- Park, T., Kashyap, V. L., Siemiginowska, A., van Dyk, D. A., Zezas, A., Heinke, C., & Wargelin, B. J. 2006, *ApJ*, 652, 610
- Persic, M., & Rephaeli, Y. 2007, *A&A*, 463, 481
- Persic, M., Rephaeli, Y., Braito, V., Cappi, M., Della Ceca, R., Franceschini, A., & Gruber, D. E. 2004, *A&A*, 419, 849
- Ranalli, P., Comastri, A., & Setti, G. 2003, *A&A*, 399, 39
- Rigby, J. R., Rieke, G. H., Donley, J. L., Alonso-Herrero, A., & Pérez-González, P. G. 2006, *ApJ*, 645, 115
- Risaliti, G., Maiolino, R., & Salvati, M. 1999, *ApJ*, 522, 157
- Rola, C. S., Terlevich, E., & Terlevich, R. J. 1997, *MNRAS*, 289, 419
- Rovilos, E., Georgantopoulos, I., Tzanavaris, P., Pracy, M., Whiting, M., Woods, D., & Goudis, C. 2009, *A&A*, 502, 85
- Sánchez, S. F., et al. 2004, *ApJ*, 614, 586
- Sarzi, M., et al. 2010, *MNRAS*, 402, 2187
- Shields, J. C., et al. 2007, *ApJ*, 654, 125
- Silverman, J. D., et al. 2008, *ApJ*, 675, 1025
- . 2009, *ApJ*, 696, 396
- Stasińska, G., Cid Fernandes, R., Mateus, A., Sodr e, L., & Asari, N. V. 2006, *MNRAS*, 371, 972
- Stern, D., et al. 2005, *ApJ*, 631, 163
- Sutherland, W., & Saunders, W. 1992, *MNRAS*, 259, 413
- Szokoly, G. P., et al. 2004, *ApJS*, 155, 271
- Treister, E., et al. 2009, *ApJ*, 706, 535
- Trouille, L., Barger, A. J., Cowie, L. L., Yang, Y., & Mushotzky, R. F. 2009, *ApJ*, 703, 2160
- Trump, J. R., et al. 2009a, *ApJ*, 696, 1195
- . 2009b, *ApJ*, 706, 797
- van Dokkum, P. G., & Franx, M. 2001, *ApJ*, 553, 90
- Veilleux, S., & Osterbrock, D. E. 1987, *ApJS*, 63, 295
- Weiner, B. J., et al. 2007, *ApJ*, 660, L39
- . 2009, *ApJ*, 692, 187
- Willmer, C. N. A., et al. 2006, *ApJ*, 647, 853
- Yan, R., Newman, J. A., Faber, S. M., Konidaris, N., Koo, D., & Davis, M. 2006, *ApJ*, 648, 281
- Yan, R., et al. 2009, *MNRAS*, 398, 735
- York, D. G., et al. 2000, *AJ*, 120, 1579
- Yuan, F., & Narayan, R. 2004, *ApJ*, 612, 724

TABLE 4 OPTICAL PROPERTIES OF ALL X-RAY SOURCES AND OPTICALLY CLASSIFIED AGNs IN OUR SAMPLE

EGSAGN No	LNG2009 ID (1)	DEEP2 ObjNo (2)	RA (J2000)	Dec	z	Mag I	$U - B$	$\log F_{[\text{O III}]}$ (erg/s/cm ²)	$\log F_{\text{H}\beta}$ (erg/s/cm ²)	$\log([\text{O III}]/\text{H}\beta)$	Survey (3)	Classification (4)
1	egs_0079	11007255	213.82423	51.97931	0.6505	20.51	1.17	-16.41 ± 0.14	< -16.75	> 0.34	1	AGN-2
2		11007325	213.81808	51.98800	0.5308	20.58	1.23	-16.44 ± 0.20	< -16.63	> 0.15	1	AGN-2
3		11007338	213.86714	51.97939	0.4278	19.97	1.20	-16.40 ± 0.17	< -16.62	> 0.21	1	AGN-2
4		11007806	213.79913	52.01271	0.5152	20.57	1.26	-16.52 ± 0.19	< -16.77	> 0.23	1	AGN-2
5		11013115	213.95496	52.05116	0.6227	21.08	0.80	-16.24 ± 0.07	-16.64 ± 0.21	0.45	1	AGN-2
6	egs_0177	11013281	213.97916	52.05984	0.4477	19.49	1.06	< -16.25	< -16.61	...	2	XBONG
7	egs_0107	11013724	213.88416	52.06547	0.6498	21.04	0.89	< -16.53	< -16.58	...	1	XBONG
8		11013883	213.81531	52.06502	0.6934	20.65	1.04	-15.75 ± 0.03	< -16.84	> 1.19	1	AGN-2
9		11013927	213.88490	52.03782	0.6508	20.97	1.08	-16.53 ± 0.17	< -16.82	> 0.27	1	AGN-2
10		11014386	213.75487	52.05908	0.4263	19.18	1.15	-16.87 ± 0.21	< -17.03	> 0.14	1	AGN-2
11		11014633	213.63841	52.04876	0.7740	20.66	1.02	-15.11 ± 0.02	-15.91 ± 0.10	> 0.88	1	AGN-2
12	egs_0017	11014774	213.66005	52.02282	0.4256	18.88	1.15	-15.94 ± 0.11	< -16.25	> 0.34	1	AGN-2
13		11014867	213.63736	52.05009	0.4831	20.69	0.96	-15.76 ± 0.09	-16.10 ± 0.11	0.38	2	AGN-2
14		11015337	213.57372	52.06427	0.7736	21.28	1.10	-15.77 ± 0.04	-16.40 ± 0.21	0.64	1	AGN-2
15	egs_0227	11019188	214.06586	52.10371	0.6313	20.26	0.65	-15.76 ± 0.05	-16.23 ± 0.12	0.41	1	AGN-1
16	egs_0150	11019509	213.95048	52.09758	0.5144	21.38	1.29	< -16.44	< -16.63	...	2	XBONG
17		11019696	213.95953	52.12963	0.6007	20.53	0.98	-16.46 ± 0.15	< -16.69	> 0.26	1	AGN-2
18		11020249	213.87015	52.10292	0.5101	20.40	1.19	-16.54 ± 0.17	< -16.85	> 0.32	1	AGN-2
19		11020265	213.84798	52.09239	0.4827	19.82	1.20	-15.63 ± 0.04	-16.22 ± 0.09	0.59	1	AGN-2
20	egs_0102	11020282	213.87775	52.07768	0.6469	19.40	0.23	-15.35 ± 0.03	-15.88 ± 0.04	0.47	2	AGN-1
21	egs_0068	11020532	213.79018	52.11860	0.5171	20.56	1.27	< -16.46	-16.59 ± 0.14	< 0.13	1	Ambiguous
22	egs_0053	11020760	213.75159	52.11627	0.4240	18.64	-0.09	-15.06 ± 0.01	-15.26 ± 0.01	0.13	2	AGN-1
23		11021077	213.67468	52.08475	0.7386	21.20	0.86	-16.60 ± 0.11	< -17.04	> 0.45	1	AGN-2
24		11021263	213.67097	52.11546	0.6186	21.53	1.28	-16.97 ± 0.20	< -16.97	> -0.01	1	AGN-2
25	egs_0005	11021753	213.59628	52.11908	0.6885	21.28	0.60	-16.26 ± 0.13	-16.13 ± 0.07	-0.14	1	SF+AGN
26		11025294	214.11182	52.17498	0.7608	20.60	0.90	-16.00 ± 0.15	-16.47 ± 0.18	0.35	1	AGN-2
27	egs_0210	11025464	214.03937	52.18389	0.6380	20.95	1.27	-16.72 ± 0.13	< -17.11	> 0.37	1	AGN-2
28		11025775	214.05022	52.16727	0.5407	21.30	0.58	-15.83 ± 0.01	< -17.02	> 1.69	1	AGN-2
29		11025795	214.09024	52.13582	0.6386	19.22	1.26	-16.02 ± 0.07	< -16.63	> 0.59	1	AGN-2
30	egs_0195	11025812	214.01665	52.18169	0.5155	21.69	0.89	-16.70 ± 0.21	< -17.02	> 0.32	1	Ambiguous
31	egs_0157	11026433	213.96178	52.15832	0.6206	20.37	1.17	-15.07 ± 0.02	-15.89 ± 0.10	0.91	1	AGN-2
32	egs_0146	11026452	213.94884	52.14548	0.6191	20.12	1.08	-15.81 ± 0.07	< -16.24	> 0.47	1	AGN-2
33		11026454	213.91220	52.14373	0.4196	19.62	1.22	-16.41 ± 0.17	< -16.62	> 0.20	1	AGN-2
34		11026737	213.84035	52.15636	0.7557	20.99	0.82	-16.22 ± 0.11	< -16.58	> 0.46	1	AGN-2
35	egs_0082	11026895	213.82692	52.18715	0.6200	21.07	1.03	-15.63 ± 0.03	-16.45 ± 0.21	0.86	1	AGN-2
36	egs_0041	11027275	213.72229	52.17474	0.4853	18.87	...	< -16.23	< -16.46	...	2	Gal
37	egs_0054	11027486	213.75434	52.17509	0.4862	21.44	1.14	< -16.63	< -16.86	...	2	XBONG
38	egs_0062	11027515	213.77725	52.18101	0.7377	21.08	0.86	-16.37 ± 0.13	-16.15 ± 0.06	-0.18	1	SF+AGN
39		11027550	213.74207	52.15421	0.4837	20.82	1.18	-16.26 ± 0.07	-16.80 ± 0.14	0.56	1	AGN-2
40		11027553	213.72713	52.15293	0.4830	19.01	1.23	-15.73 ± 0.05	-15.91 ± 0.05	0.18	1	AGN-2
41		11027572	213.72940	52.13875	0.4815	20.75	1.07	-16.65 ± 0.18	< -16.93	> 0.28	1	AGN-2
42		11027926	213.71576	52.18502	0.5711	21.41	1.18	-16.03 ± 0.10	< -16.66	> 0.67	1	AGN-2
43	egs_0011	11027995	213.63187	52.18433	0.8054	20.86	1.06	-16.36 ± 0.18	< -16.56	> 0.22	1	AGN-2
44		11028015	213.63812	52.14281	0.7717	20.89	1.17	-16.02 ± 0.06	< -16.61	> 0.61	1	AGN-2
45		11028069	213.69270	52.15824	0.3581	18.60	1.22	-16.35 ± 0.16	-16.50 ± 0.18	0.16	1	AGN-2
46	egs_0329	11031536	214.24285	52.20145	0.6020	19.78	0.37	-15.29 ± 0.03	-16.31 ± 0.13	0.97	2	AGN-1
47	egs_0292	11032099	214.18018	52.24328	0.5302	20.06	0.47	-14.92 ± 0.03	-16.21 ± 0.15	1.26	2	AGN-1
48		11032166	214.16151	52.19590	0.3797	21.18	1.14	-16.65 ± 0.19	< -16.78	> 0.20	1	AGN-2
49	egs_0239	11032690	214.07687	52.22640	0.6400	20.77	1.20	-16.47 ± 0.14	< -16.66	> 0.15	1	AGN-2
50		11032728	214.08510	52.23033	0.3660	18.46	1.23	-16.13 ± 0.11	-16.36 ± 0.12	0.22	1	AGN-2
51	egs_0182	11033336	213.98689	52.21817	0.5157	20.19	1.46	< -16.05	< -16.43	...	1	XBONG
52		11033376	213.95151	52.19230	0.5067	20.13	1.10	-15.48 ± 0.06	-16.23 ± 0.20	> 0.73	2	AGN-2
53	egs_0081	11033890	213.82550	52.20644	0.6917	21.04	0.63	-16.29 ± 0.21	< -16.63	> 0.36	2	AGN-1
54	egs_0103	11033900	213.88078	52.19598	0.4195	19.32	1.15	-16.18 ± 0.14	-16.37 ± 0.18	0.20	1	AGN-2
55		11034196	213.78416	52.22329	0.5315	20.06	1.09	-15.93 ± 0.17	< -16.24	> 0.29	1	AGN-2
56		11034392	213.72045	52.21359	0.3005	18.64	1.08	-16.11 ± 0.20	< -16.31	> 0.20	2	AGN-2
57	egs_0024	11034896	213.68194	52.20096	0.5168	19.67	0.93	-15.72 ± 0.20	< -15.98	> 0.29	2	AGN-2
58		11037823	214.31896	52.26043	0.4161	20.85	1.22	-16.23 ± 0.18	< -16.53	> 0.22	2	AGN-2
59		11037887	214.33244	52.28719	0.6842	21.75	0.85	-16.11 ± 0.06	-16.70 ± 0.11	> 0.53	1	AGN-2
60	egs_0311	11038266	214.21049	52.27648	0.6829	20.99	1.19	-15.94 ± 0.04	< -16.94	> 1.04	1	AGN-2
61	egs_0309	11038472	214.20647	52.28167	0.7615	21.01	0.75	-16.46 ± 0.16	-16.16 ± 0.05	-0.26	1	SF+AGN
62	egs_0310	11038492	214.20802	52.30260	0.8081	20.96	0.96	-16.07 ± 0.07	-16.36 ± 0.07	0.29	1	AGN-2
63		11038502	214.20409	52.29402	0.3658	18.51	1.21	-16.49 ± 0.16	< -16.76	> 0.28	1	AGN-2
64		11038552	214.25833	52.26073	0.5085	19.77	1.32	-16.48 ± 0.21	< -16.48	> 0.03	1	AGN-2
65		11039110	214.16689	52.29306	0.5327	19.23	1.29	-16.64 ± 0.20	< -16.90	> 0.24	1	AGN-2
66		11039115	214.18024	52.28918	0.4510	19.55	1.26	-15.86 ± 0.07	-16.48 ± 0.16	0.58	1	AGN-2

X-ray vs. optical selection of AGNs

Continued on Next Page...

EGSAGN No	LNG2009 ID (1)	DEEP2 ObjNo (2)	RA (J2000)	Dec	z	Mag I	$U - B$	$\log F_{[\text{O III}]}$ (erg/s/cm ²)	$\log F_{\text{H}\beta}$ (erg/s/cm ²)	$\log([\text{O III}]/\text{H}\beta)$	Survey (3)	Classification (4)
67		11039152	214.17536	52.26902	0.4325	20.57	0.81	-15.55 ± 0.10	-16.07 ± 0.17	0.52	2	AGN-2
68	egs_0271	11039155	214.14906	52.26676	0.5073	20.79	0.59	-16.04 ± 0.05	-16.07 ± 0.05	0.01	1	SF+AGN
69	egs_0215	11039717	214.04414	52.27272	0.4206	19.37	1.28	-16.16 ± 0.20	< -16.35	> 0.18	2	AGN-2
70		11040226	213.96581	52.30114	0.4518	20.48	1.00	-15.70 ± 0.05	-16.24 ± 0.09	0.50	1	AGN-2
71		11040258	213.94131	52.28044	0.4195	19.57	1.22	-16.30 ± 0.11	< -16.73	> 0.41	1	AGN-2
72		11040856	213.86661	52.24823	0.6476	20.90	1.28	-16.61 ± 0.21	< -16.74	> 0.11	1	AGN-2
73	egs_0394	11043955	214.39114	52.34441	0.4350	20.36	0.96	-15.93 ± 0.05	-16.28 ± 0.08	0.36	2	AGN-2
74		11044264	214.33392	52.34035	0.4503	20.40	0.61	-14.70 ± 0.01	-15.58 ± 0.02	> 0.89	1	AGN-2
75	egs_0353	11044654	214.29948	52.33668	0.4334	19.32	0.73	-15.14 ± 0.03	< -16.32	> 1.17	1	AGN-2
76	egs_0361	11044672	214.31410	52.32079	0.4174	19.39	1.15	-16.04 ± 0.10	-16.45 ± 0.19	> 0.41	2	AGN-2
77		11044822	214.24783	52.31716	0.4177	20.46	1.14	-16.87 ± 0.21	< -16.96	> 0.08	1	AGN-2
78		11045101	214.22156	52.34466	0.5071	20.52	1.25	-16.44 ± 0.09	< -16.88	> 0.43	1	AGN-2
79	egs_0333	11045238	214.25285	52.32184	0.4187	19.79	0.63	-15.32 ± 0.03	-15.85 ± 0.06	0.59	2	AGN-1
80		11045833	214.10196	52.35545	0.4835	20.97	1.12	-15.48 ± 0.03	-16.61 ± 0.14	1.23	1	AGN-2
81		11045870	214.17010	52.33091	0.3792	20.47	1.22	-16.73 ± 0.20	-16.88 ± 0.20	0.15	1	AGN-2
82	egs_0267	11045881	214.14430	52.32461	0.7042	21.55	0.91	-16.32 ± 0.08	< -16.75	> 0.42	1	AGN-2
83		11045898	214.15665	52.30989	0.4787	20.56	1.23	-16.77 ± 0.21	< -17.02	> 0.25	1	AGN-2
84		11046075	214.04321	52.33386	0.8099	21.86	1.01	-16.52 ± 0.14	< -16.92	> 0.41	1	AGN-2
85	egs_0223	11046217	214.06060	52.32884	0.6827	21.23	0.72	< -16.22	< -16.64	...	2	XBONG
86	egs_0205	11046398	214.03516	52.35761	0.6156	19.92	0.99	< -16.37	< -16.39	...	1	XBONG
87	egs_0218	11046428	214.05270	52.35726	0.3309	19.97	0.84	-14.95 ± 0.01	-15.90 ± 0.03	1.02	1	AGN-2
88		11046450	214.08952	52.34215	0.5315	21.06	1.27	-16.66 ± 0.18	< -16.90	> 0.26	1	AGN-2
89	egs_0201	11046507	214.02075	52.30777	0.4516	20.52	0.31	-14.82 ± 0.01	-15.33 ± 0.01	> 0.49	2	SF+AGN
90		11046512	214.04793	52.30590	0.5102	19.99	1.23	-16.48 ± 0.14	< -16.92	> 0.44	1	AGN-2
91	egs_0139	11047040	213.94314	52.35420	0.4506	19.71	1.08	< -16.34	< -16.67	...	2	XBONG
92	egs_0161	11047085	213.96347	52.32336	0.6209	20.68	1.06	-14.89 ± 0.01	-15.98 ± 0.04	1.10	1	AGN-2
93		11047626	213.88997	52.34827	0.6476	19.60	0.99	-15.76 ± 0.03	< -16.76	> 1.02	1	AGN-2
94		11050860	214.41101	52.38120	0.3852	21.50	0.98	-16.02 ± 0.05	-16.59 ± 0.10	0.56	1	AGN-2
95	egs_0289	11052008	214.17773	52.39020	0.5148	19.49	1.19	-16.24 ± 0.19	< -16.52	> 0.26	1	AGN-2
96	egs_0276	11052013	214.15884	52.38577	0.4170	19.44	1.20	< -16.45	< -16.52	...	1	XBONG
97	egs_0295	11052031	214.18341	52.37200	0.5104	19.64	1.15	-15.42 ± 0.03	-16.29 ± 0.10	0.86	1	AGN-2
98	egs_0237	11052379	214.07619	52.39520	0.4822	19.80	0.90	-16.37 ± 0.14	-15.86 ± 0.03	-0.50	1	SF+AGN
99	egs_0232	11052423	214.07011	52.36295	0.4825	19.35	1.15	-16.58 ± 0.21	-16.53 ± 0.13	-0.04	1	SF+AGN
100	egs_0144	11052713	213.94736	52.40224	0.5233	20.53	0.84	-16.20 ± 0.11	-16.08 ± 0.05	-0.14	1	SF+AGN
101		11101177	213.87749	52.27689	0.7031	21.74	1.09	-15.55 ± 0.03	-16.55 ± 0.17	1.04	1	AGN-2
102		11101582	213.94656	52.23082	0.7378	20.51	1.14	-15.78 ± 0.10	-15.96 ± 0.10	0.17	1	AGN-2
103		12000755	214.54271	52.37595	0.4171	21.04	1.01	-14.90 ± 0.04	-15.94 ± 0.09	1.10	2	AGN-2
104		12003742	214.44595	52.41988	0.7486	21.37	1.19	-15.81 ± 0.04	-16.71 ± 0.12	0.87	1	AGN-2
105		12003798	214.45955	52.44389	0.5488	20.88	1.00	-16.02 ± 0.06	-16.54 ± 0.11	0.54	1	AGN-2
106	egs_0439	12003821	214.46260	52.42623	0.4315	20.33	1.07	-16.59 ± 0.13	< -16.95	> 0.37	1	AGN-2
107		12004071	214.34865	52.41991	0.4636	20.41	1.23	-15.93 ± 0.17	< -16.50	> 0.53	2	AGN-2
108		12004106	214.38005	52.44333	0.7436	20.70	1.26	-16.58 ± 0.20	< -16.77	> 0.20	1	AGN-2
109	egs_0351	12004491	214.29613	52.42803	0.4184	19.28	1.21	< -16.32	< -16.52	...	2	XBONG
110		12004496	214.31384	52.42586	0.5314	19.73	1.32	-16.35 ± 0.12	< -16.80	> 0.43	1	AGN-2
111		12004511	214.27477	52.41318	0.5804	20.56	1.26	-16.48 ± 0.14	< -16.90	> 0.43	1	AGN-2
112	egs_0345	12004519	214.28688	52.40828	0.4510	20.80	0.52	-15.08 ± 0.03	-15.57 ± 0.03	0.50	2	SF+AGN
113		12005147	214.06236	52.42713	0.3556	19.31	1.14	-16.16 ± 0.15	< -16.39	> 0.21	1	AGN-2
114	egs_0194	12005349	214.00380	52.40665	0.6032	20.75	0.87	-15.32 ± 0.02	-16.05 ± 0.05	0.77	1	AGN-2
115		12005433	214.01035	52.40566	0.7668	21.15	1.10	-15.69 ± 0.05	-16.35 ± 0.11	0.70	1	AGN-2
116		12005560	214.04204	52.40986	0.4418	20.13	1.21	-16.41 ± 0.12	< -16.77	> 0.35	1	AGN-2
117	egs_0148	12005778	213.94963	52.41837	0.6716	20.93	0.73	-16.16 ± 0.09	-16.05 ± 0.04	-0.09	1	SF+AGN
118		12007534	214.57448	52.47220	0.7170	21.26	0.85	-16.04 ± 0.09	-16.49 ± 0.14	0.41	1	AGN-2
119		12007579	214.53687	52.47486	0.6573	21.35	0.87	-16.33 ± 0.13	< -16.70	> 0.41	1	AGN-2
120	egs_0445	12007896	214.47087	52.47754	0.6711	20.73	0.71	-16.26 ± 0.13	-16.03 ± 0.05	-0.23	1	SF+AGN
121	egs_0374	12008225	214.35263	52.50690	0.4818	19.66	0.29	-15.61 ± 0.01	< -17.22	> 1.55	1	AGN-1
122		12008603	214.26804	52.45736	0.4191	21.00	1.18	-16.88 ± 0.21	< -16.90	> 0.05	1	AGN-2
123	egs_0346	12008608	214.28719	52.45261	0.5319	19.80	1.19	-16.35 ± 0.12	< -16.85	> 0.49	1	AGN-2
124		12009257	214.07956	52.49295	0.3527	19.25	1.17	-16.48 ± 0.16	< -16.56	> 0.11	1	AGN-2
125		12009287	214.07515	52.46996	0.4662	21.21	0.85	-16.60 ± 0.15	< -16.97	> 0.39	1	AGN-2
126	egs_0610	12011424	214.67381	52.53200	0.6849	20.67	1.30	< -16.03	< -16.11	...	2	XBONG
127		12011465	214.66512	52.55250	0.5339	21.34	1.14	-16.76 ± 0.19	< -17.03	> 0.28	1	AGN-2
128		12012451	214.38219	52.55571	0.5706	20.87	1.25	-16.34 ± 0.14	< -16.57	> 0.22	1	AGN-2
129	egs_0370	12012471	214.34766	52.53162	0.4836	20.85	0.49	-15.79 ± 0.03	-16.35 ± 0.05	0.54	1	AGN-1
130	egs_0369	12012474	214.34576	52.52883	0.4647	20.67	0.92	-15.30 ± 0.02	-16.36 ± 0.06	1.08	1	AGN-2
131	egs_0393	12012543	214.39099	52.56374	0.5506	20.61	0.75	-15.46 ± 0.03	-15.92 ± 0.04	0.46	1	SF+AGN
132		12012566	214.35150	52.53736	0.4825	19.20	1.03	-15.65 ± 0.05	-16.42 ± 0.18	> 0.76	1	AGN-2
133		12012848	214.26193	52.54360	0.5321	20.88	0.98	-16.45 ± 0.21	< -16.71	> 0.27	1	AGN-2
134	egs_0287	12013154	214.17487	52.52867	0.6044	20.21	1.00	-15.21 ± 0.01	-16.44 ± 0.08	1.26	1	AGN-2
135		12015292	214.76270	52.62329	0.5493	20.65	1.33	-16.48 ± 0.18	< -16.74	> 0.26	1	AGN-2
136		12015645	214.68488	52.59996	0.6849	21.22	1.28	-16.76 ± 0.17	< -17.08	> 0.31	1	AGN-2

Continued on Next Page...

EGSAGN No	LNG2009 ID (1)	DEEP2 ObjNo (2)	RA (J2000)	Dec	<i>z</i>	Mag <i>I</i>	<i>U</i> - <i>B</i>	$\log F_{[\text{O III}]}$ (erg/s/cm ²)	$\log F_{\text{H}\beta}$ (erg/s/cm ²)	$\log([\text{O III}]/\text{H}\beta)$	Survey (3)	Classification (4)
137		12015657	214.67033	52.57345	0.4222	19.82	1.15	-16.68 ± 0.22	< -16.80	> 0.11	1	AGN-2
138		12015978	214.58771	52.61986	0.4208	20.66	1.22	-16.86 ± 0.19	< -16.97	> 0.12	1	AGN-2
139		12016021	214.56915	52.61103	0.7133	20.57	1.32	-16.65 ± 0.20	-16.70 ± 0.16	> 0.04	1	AGN-2
140	egs_0447	12016316	214.47377	52.57961	0.7188	21.60	0.83	-16.04 ± 0.13	< -16.50	> 0.48	1	AGN-2
141		12016405	214.47258	52.59439	0.6791	20.22	1.31	-16.66 ± 0.19	< -16.93	> 0.29	1	AGN-2
142	egs_0407	12016714	214.41045	52.62378	0.4248	21.56	0.96	< -16.70	-16.77 ± 0.19	< 0.07	2	Blended
143	egs_0390	12016790	214.38541	52.57811	0.4646	19.59	0.56	-15.55 ± 0.03	-15.39 ± 0.01	-0.14	1	SF+AGN
144	egs_0705	12019136	214.84639	52.67060	0.7340	21.58	1.04	-15.42 ± 0.05	-16.30 ± 0.11	0.85	1	AGN-2
145	egs_0699	12019186	214.83585	52.66637	0.4885	20.75	0.68	-15.76 ± 0.04	-16.47 ± 0.16	0.70	1	AGN-1
146	egs_0726	12019189	214.87509	52.66192	0.5510	20.21	1.29	-15.78 ± 0.11	< -16.41	> 0.65	2	AGN-2
147		12019603	214.75455	52.66646	0.6783	20.77	1.22	-16.40 ± 0.18	< -16.74	> 0.32	1	AGN-2
148		12019616	214.75995	52.64568	0.5827	20.39	1.25	-16.04 ± 0.06	< -16.82	> 0.82	1	AGN-2
149		12019630	214.72545	52.62502	0.5503	20.41	1.26	-16.32 ± 0.18	< -16.75	> 0.43	2	AGN-2
150	egs_0585	12019829	214.63342	52.66808	0.5701	21.73	1.20	< -16.73	< -16.77	...	1	XBONG
151		12020007	214.69838	52.67864	0.7217	21.18	1.07	-16.11 ± 0.09	-16.36 ± 0.11	0.29	1	AGN-2
152		12020010	214.64638	52.67614	0.5706	19.66	1.36	-16.56 ± 0.19	< -16.74	> 0.19	1	AGN-2
153		12020437	214.59518	52.63941	0.5807	20.02	0.94	-15.64 ± 0.03	-16.05 ± 0.04	0.45	1	AGN-2
154		12020616	214.50252	52.65271	0.3392	20.97	1.10	-16.69 ± 0.14	-16.67 ± 0.14	0.08	1	AGN-2
155	egs_0421	12020721	214.44063	52.66439	0.6979	20.91	1.30	-16.10 ± 0.18	< -16.58	> 0.38	2	AGN-2
156	egs_0392	12021115	214.38583	52.63831	0.7168	19.58	1.19	-15.75 ± 0.06	< -16.47	> 0.72	1	AGN-2
157		12021116	214.37271	52.63787	0.3556	17.90	1.26	-15.63 ± 0.04	-16.12 ± 0.08	0.50	1	AGN-2
158		12021407	214.29414	52.63745	0.5925	20.50	1.04	-15.89 ± 0.06	< -16.71	> 0.84	1	AGN-2
159		12021476	214.29625	52.62479	0.6439	20.04	1.18	-15.94 ± 0.08	-16.46 ± 0.18	0.49	1	AGN-2
160	egs_0783	12023326	214.96448	52.70131	0.5488	20.61	0.75	-15.62 ± 0.05	-16.69 ± 0.21	1.04	2	AGN-1
161	egs_0673	12024136	214.79019	52.68381	0.7288	20.45	0.83	< -16.09	-16.12 ± 0.10	< 0.03	1	SF+AGN
162	egs_0577	12024309	214.62466	52.70436	0.6435	20.24	0.86	-16.30 ± 0.13	-16.22 ± 0.08	-0.09	1	SF+AGN
163	egs_0584	12024323	214.63306	52.68759	0.5700	20.53	1.19	< -16.63	< -16.72	...	1	XBONG
164	egs_0558	12024913	214.60120	52.70196	0.7594	21.21	0.62	-16.40 ± 0.15	-16.07 ± 0.05	-0.33	1	SF+AGN
165	egs_0435	12025262	214.45734	52.73520	0.7437	20.87	0.91	-15.44 ± 0.05	-16.17 ± 0.10	0.82	2	AGN-2
166	egs_0453	12025302	214.47919	52.69567	0.4636	21.16	1.02	-15.53 ± 0.02	-16.58 ± 0.08	1.11	1	AGN-2
167		12025632	214.38924	52.71405	0.4195	20.46	0.82	-15.46 ± 0.01	-15.92 ± 0.02	0.50	1	AGN-2
168	egs_0753	12027585	214.92807	52.77725	0.7843	21.18	0.80	-15.49 ± 0.02	-16.16 ± 0.06	0.63	1	AGN-1
169		12027757	214.86462	52.78273	0.7369	21.91	0.92	-16.19 ± 0.10	< -16.85	> 0.65	1	AGN-2
170	egs_0691	12027983	214.82048	52.78252	0.4544	21.69	0.58	-15.45 ± 0.03	-15.99 ± 0.03	0.55	1	SF+AGN
171		12028910	214.52979	52.76188	0.6067	21.98	0.93	-16.48 ± 0.08	< -16.97	> 0.53	1	AGN-2
172		12029076	214.54372	52.78081	0.3535	18.93	1.13	-16.43 ± 0.15	< -16.67	> 0.26	1	AGN-2
173		12029377	214.50133	52.76718	0.6442	20.46	1.19	-15.40 ± 0.06	< -16.55	> 1.03	1	AGN-2
174		13003825	214.89467	52.82994	0.4617	19.56	1.12	-16.42 ± 0.14	< -16.86	> 0.44	1	AGN-2
175		13003865	214.86230	52.80200	0.5471	20.15	1.45	-16.43 ± 0.21	< -16.64	> 0.19	1	AGN-2
176	egs_0714	13003867	214.85877	52.79933	0.4352	19.40	1.45	< -16.57	< -16.77	...	2	XBONG
177		13004280	214.78279	52.83120	0.4409	18.50	1.07	-16.07 ± 0.11	< -16.54	> 0.47	1	AGN-2
178	egs_0677	13004312	214.79359	52.80868	0.3459	18.31	1.27	-16.31 ± 0.14	< -16.62	> 0.31	1	AGN-2
179		13004317	214.81565	52.80694	0.3464	20.14	1.06	-16.23 ± 0.17	-16.43 ± 0.19	0.16	2	AGN-2
180		13004331	214.79047	52.79341	0.3711	19.42	1.17	-16.32 ± 0.10	-16.32 ± 0.07	0.00	1	AGN-2
181	egs_0818	13009690	215.03771	52.87078	0.5422	20.43	1.15	-15.94 ± 0.18	< -16.33	> 0.50	2	AGN-2
182		13009980	215.11288	52.85669	0.4561	19.46	1.14	-15.94 ± 0.11	-16.38 ± 0.13	0.43	1	AGN-2
183		13009989	215.10619	52.85037	0.4594	19.43	1.12	-15.68 ± 0.07	-16.50 ± 0.19	0.81	2	AGN-2
184		13010501	215.01120	52.88775	0.6707	21.36	1.12	-16.29 ± 0.11	-16.81 ± 0.18	0.61	1	AGN-2
185	egs_0802	13010503	215.00620	52.88623	0.4614	21.32	1.02	-16.93 ± 0.19	< -17.29	> 0.36	1	AGN-2
186		13010507	215.01846	52.88343	0.3668	21.75	0.49	-15.27 ± 0.05	-16.47 ± 0.17	1.20	1	AGN-2
187		13010921	214.87363	52.86663	0.3690	18.73	1.15	-16.10 ± 0.11	-16.24 ± 0.10	0.15	1	AGN-2
188	egs_0724	13011062	214.87428	52.86858	0.3698	19.58	1.07	< -16.58	< -16.79	...	1	XBONG
189		13011073	214.93352	52.85826	0.7309	21.43	1.09	-16.27 ± 0.14	-16.81 ± 0.18	0.52	1	AGN-2
190		13011171	214.91618	52.87112	0.4625	20.33	1.26	-16.73 ± 0.21	< -17.02	> 0.29	1	AGN-2
191		13011196	214.90547	52.85097	0.6703	19.21	0.96	-14.66 ± 0.02	-15.75 ± 0.11	1.15	1	AGN-2
192		13011215	214.87401	52.83570	0.4620	21.05	1.19	-16.82 ± 0.20	-17.02 ± 0.16	0.18	1	AGN-2
193		13011657	214.76202	52.88325	0.4408	20.70	1.17	-16.36 ± 0.15	-16.55 ± 0.16	0.19	1	AGN-2
194	egs_0690	13011701	214.81995	52.84563	0.7403	20.73	0.88	-16.34 ± 0.10	-16.02 ± 0.04	-0.26	1	SF+AGN
195		13011758	214.80289	52.89119	0.3793	18.89	1.23	-16.25 ± 0.18	< -16.47	> 0.22	1	AGN-2
196		13011778	214.81533	52.87100	0.4518	20.08	1.16	-15.41 ± 0.03	-16.34 ± 0.08	0.95	2	AGN-2
197	egs_0692	13011817	214.82223	52.84312	0.6603	19.91	0.81	-15.16 ± 0.04	-15.91 ± 0.11	0.84	2	AGN-2
198		13011894	214.68234	52.85892	0.7618	21.62	1.19	-16.48 ± 0.19	< -16.85	> 0.35	1	AGN-2
199	egs_0618	13012268	214.68341	52.86171	0.6796	21.19	0.94	-15.50 ± 0.02	-16.40 ± 0.07	0.95	1	AGN-2
200	egs_0604	13012387	214.66362	52.86137	0.3453	18.73	1.17	-16.18 ± 0.12	-16.17 ± 0.10	0.00	1	AGN-2
201		13017117	215.14215	52.91428	0.7309	21.36	1.11	-16.32 ± 0.19	< -16.81	> 0.47	1	AGN-2
202	egs_0893	13017287	215.13574	52.94368	0.6379	21.07	1.20	-16.10 ± 0.12	< -16.51	> 0.40	1	AGN-2
203	egs_0955	13017327	215.21848	52.93956	0.6764	17.90	0.04	-14.97 ± 0.04	-15.30 ± 0.03	0.28	2	AGN-1
204		13017767	215.03967	52.93049	0.7400	21.31	1.31	-16.98 ± 0.20	-16.90 ± 0.16	0.09	1	AGN-2
205		13018001	215.05138	52.94855	0.7399	20.38	1.14	-16.33 ± 0.19	-16.38 ± 0.14	0.04	1	AGN-2
206	egs_0836	13018061	215.05704	52.90372	0.5755	20.14	0.74	-15.54 ± 0.02	-16.54 ± 0.11	1.02	1	AGN-2

Continued on Next Page...

EGSAGN No	LNG2009 ID (1)	DEEP2 ObjNo (2)	RA (J2000)	Dec	z	Mag I	$U - B$	$\log F_{[\text{O III}]}$ (erg/s/cm ²)	$\log F_{\text{H}\beta}$ (erg/s/cm ²)	$\log([\text{O III}]/\text{H}\beta)$	Survey (3)	Classification (4)
207		13018614	214.99104	52.92006	0.7478	21.60	1.07	-16.38 ± 0.21	-16.64 ± 0.20	0.23	1	AGN-2
208		13019107	214.86615	52.94028	0.5976	20.31	1.11	-16.42 ± 0.19	-16.50 ± 0.20	0.10	1	AGN-2
209		13019234	214.85989	52.94123	0.5103	20.63	1.14	-16.47 ± 0.18	-16.68 ± 0.18	0.23	1	AGN-2
210	egs_0748	13019240	214.91629	52.93751	0.7454	21.44	1.14	-16.66 ± 0.16	< -16.95	> 0.31	1	AGN-2
211	egs_0683	13019868	214.80713	52.89747	0.5364	20.18	0.88	-15.20 ± 0.01	-16.22 ± 0.06	1.09	1	AGN-2
212	egs_0702	13019950	214.84204	52.92208	0.7690	20.86	1.08	-15.18 ± 0.02	-16.16 ± 0.06	1.05	1	AGN-2
213		13019984	214.80457	52.89635	0.5359	19.51	0.69	-16.36 ± 0.08	< -16.95	> 0.60	1	AGN-2
214		13020541	214.66305	52.94496	0.5827	19.07	0.85	-15.93 ± 0.22	< -16.30	> 0.41	2	AGN-2
215		13020619	214.72878	52.89186	0.4414	19.71	1.25	-16.35 ± 0.09	< -16.82	> 0.47	1	AGN-2
216		13024002	215.33495	52.98376	0.4471	20.92	0.89	-16.04 ± 0.13	-16.60 ± 0.17	> 0.54	2	AGN-2
217		13025397	215.19727	52.97180	0.7363	20.37	1.24	-16.42 ± 0.16	< -16.77	> 0.33	1	AGN-2
218	egs_0924	13025417	215.17453	52.95694	0.7451	20.77	1.20	-16.35 ± 0.10	-16.42 ± 0.08	0.05	1	AGN-2
219		13025437	215.14026	52.98820	0.7105	21.26	1.38	-15.45 ± 0.02	-16.60 ± 0.16	1.15	1	AGN-2
220		13025468	215.18042	52.99598	0.3509	18.51	1.15	-16.12 ± 0.18	< -16.34	> 0.22	2	AGN-2
221	egs_0943	13025494	215.20303	52.97853	0.7386	21.17	1.19	-16.40 ± 0.13	-16.61 ± 0.13	0.17	1	AGN-2
222		13025503	215.13287	52.97287	0.3789	18.95	1.17	-16.45 ± 0.14	< -16.80	> 0.34	1	AGN-2
223	egs_0898	13025514	215.13948	52.96697	0.5699	19.47	1.26	< -16.50	< -16.59	...	1	Gal
224		13025741	215.11980	52.97969	0.7789	21.32	1.25	-16.76 ± 0.19	< -16.82	> 0.05	1	AGN-2
225	egs_0861	13026185	215.08670	52.97848	0.6312	21.11	1.13	< -16.83	< -16.74	...	1	XBONG
226	egs_0871	13026227	215.09863	52.95120	0.4622	19.54	1.01	< -16.46	-16.31 ± 0.10	< -0.14	1	SF+AGN
227		13026727	215.00008	52.98274	0.7435	21.77	1.00	-15.83 ± 0.03	-16.65 ± 0.11	0.88	1	AGN-2
228		13026882	215.01663	52.95243	0.3540	19.84	1.06	-16.73 ± 0.17	< -16.90	> 0.19	1	AGN-2
229	egs_0725	13027442	214.87381	52.95618	0.7676	20.48	1.29	< -16.61	< -16.80	...	1	XBONG
230		13027882	214.79909	52.96043	0.5714	19.86	1.17	-15.26 ± 0.08	< -16.06	> 0.84	2	AGN-2
231		13028108	214.79341	52.98073	0.3580	19.67	1.07	-16.37 ± 0.11	-16.49 ± 0.12	0.12	1	AGN-2
232		13028128	214.76411	52.96373	0.6561	19.54	1.28	-16.19 ± 0.18	< -16.55	> 0.36	1	AGN-2
233		13032374	215.34123	53.03220	0.7320	19.86	1.14	-15.85 ± 0.17	-16.15 ± 0.15	0.24	1	AGN-2
234		13032376	215.32700	53.03075	0.7320	21.03	1.08	-15.92 ± 0.10	-16.38 ± 0.11	0.43	1	AGN-2
235	egs_1027	13032511	215.32881	53.00916	0.7395	21.79	0.78	-16.28 ± 0.07	-16.41 ± 0.06	0.11	1	SF+AGN
236	egs_0996	13033068	215.28231	53.05504	0.7368	21.15	0.34	-16.30 ± 0.17	-16.79 ± 0.18	0.42	2	AGN-1
237	egs_1013	13033179	215.31338	53.05981	0.7394	21.67	0.43	-16.37 ± 0.12	-16.43 ± 0.19	0.26	2	SF+AGN
238		13033207	215.31697	53.03967	0.3778	19.00	1.17	-16.26 ± 0.10	-16.59 ± 0.14	0.33	1	AGN-2
239	egs_0989	13033215	215.27125	53.03537	0.7392	20.22	1.33	< -15.97	< -16.00	...	2	Gal
240	egs_0934	13033778	215.18931	53.05824	0.3787	18.87	1.22	< -16.43	< -16.67	...	2	XBONG
241		13033927	215.21864	53.03823	0.7349	21.60	1.22	-16.10 ± 0.09	< -16.82	> 0.70	1	AGN-2
242		13033952	215.18712	53.02296	0.4329	19.64	1.12	-16.37 ± 0.12	-16.46 ± 0.12	0.11	1	AGN-2
243		13033958	215.16339	53.02019	0.3666	19.76	1.10	-16.67 ± 0.17	< -16.94	> 0.28	1	AGN-2
244	egs_0839	13034447	215.06064	53.02398	0.7482	20.91	1.10	< -16.90	< -17.09	...	1	XBONG
245		13034610	215.12338	53.03746	0.3478	19.71	1.17	-16.77 ± 0.16	< -16.97	> 0.21	1	AGN-2
246	egs_0851	13034618	215.07686	53.03268	0.3557	19.13	1.15	-16.11 ± 0.06	< -16.80	> 0.69	1	AGN-2
247		13034622	215.12186	53.02950	0.4329	19.97	1.20	-16.82 ± 0.19	< -17.02	> 0.20	1	AGN-2
248	egs_0782	13035250	214.96342	53.01241	0.7444	19.82	1.16	-15.93 ± 0.11	-16.30 ± 0.16	0.35	1	AGN-2
249		13035323	214.96506	53.01800	0.7462	21.37	0.99	-16.32 ± 0.09	-16.56 ± 0.09	0.25	1	AGN-2
250	egs_0716	13035554	214.86077	53.03118	0.6724	21.02	1.33	-15.61 ± 0.11	< -16.47	> 0.80	2	AGN-2
251		13035739	214.91626	53.02839	0.4562	20.53	1.06	-15.79 ± 0.03	-15.99 ± 0.03	0.22	1	AGN-2
252		13035831	214.85316	53.01901	0.6782	21.79	1.01	-16.67 ± 0.14	< -17.04	> 0.42	1	AGN-2
253		13035860	214.91283	53.03973	0.7629	21.61	1.05	-16.37 ± 0.13	< -16.90	> 0.53	1	AGN-2
254	egs_0735	13035954	214.89311	53.05591	0.6110	20.56	1.16	-16.22 ± 0.07	-16.72 ± 0.14	0.50	1	AGN-2
255		13035995	214.86253	53.03141	0.5106	21.09	0.95	-16.51 ± 0.09	-16.91 ± 0.14	0.42	1	AGN-2
256		13036013	214.87405	53.01782	0.6777	19.65	1.10	-15.37 ± 0.09	-15.89 ± 0.18	0.58	1	AGN-2
257		13036642	214.82635	53.02877	0.4195	20.35	1.16	-16.68 ± 0.17	< -16.87	> 0.19	1	AGN-2
258	egs_0667	13036677	214.78314	53.00728	0.5630	20.10	0.66	-15.75 ± 0.04	-16.39 ± 0.16	0.65	1	AGN-1
259	egs_1157	13039488	215.53809	53.09995	0.7575	19.40	0.48	-15.25 ± 0.04	< -16.50	> 1.23	2	AGN-1
260		13040160	215.50137	53.11680	0.4586	20.06	1.16	-16.78 ± 0.18	< -17.07	> 0.28	1	AGN-2
261	egs_1105	13040188	215.46159	53.09480	0.3901	19.43	1.22	-16.51 ± 0.12	-15.97 ± 0.05	-0.40	1	SF+AGN
262		13040619	215.37157	53.09986	0.7109	21.46	1.23	-16.77 ± 0.13	-16.84 ± 0.15	0.06	1	AGN-2
263		13040675	215.38112	53.07705	0.4179	21.46	0.87	-15.98 ± 0.04	-16.45 ± 0.07	0.50	1	AGN-2
264		13040854	215.32623	53.09688	0.4354	20.86	0.86	-16.40 ± 0.11	< -16.76	> 0.39	1	AGN-2
265		13040894	215.36708	53.10523	0.7092	20.51	1.18	-16.56 ± 0.14	-16.71 ± 0.19	0.14	1	AGN-2
266		13040903	215.37381	53.10111	0.5312	21.10	1.02	-15.96 ± 0.05	-16.22 ± 0.06	0.30	1	AGN-2
267	egs_1044	13040957	215.35161	53.06601	0.6779	20.22	1.04	< -15.62	< -16.13	...	2	XBONG
268		13042327	215.20277	53.10669	0.3546	18.89	1.33	-15.99 ± 0.07	< -16.61	> 0.62	1	AGN-2
269		13042335	215.22481	53.10232	0.3545	19.97	1.14	-16.59 ± 0.14	< -16.86	> 0.28	1	AGN-2
270	egs_0889	13042341	215.13486	53.09865	0.4345	20.03	1.19	< -16.80	< -16.88	...	1	XBONG
271	egs_0819	13043031	215.03812	53.10342	0.7633	21.83	1.15	< -16.62	< -16.74	...	1	XBONG
272		13043673	214.94967	53.11792	0.7466	20.61	0.60	-15.70 ± 0.08	< -16.42	> 0.77	2	AGN-2
273		13043702	214.98361	53.09675	0.3547	19.08	1.14	-16.38 ± 0.16	-16.42 ± 0.14	0.07	1	AGN-2
274		13047962	215.55843	53.15877	0.6915	21.81	0.62	-15.48 ± 0.02	-16.37 ± 0.05	0.88	1	AGN-2
275		13048575	215.44892	53.17318	0.6787	20.53	1.28	-15.69 ± 0.18	< -16.24	> 0.57	2	AGN-2
276	egs_1030	13049115	215.33679	53.12429	0.4655	20.22	0.68	-15.71 ± 0.05	-15.81 ± 0.04	0.13	1	SF+AGN

Continued on Next Page...

EGSAGN No	LNG2009 ID (1)	DEEP2 ObjNo (2)	RA (J2000)	Dec	z	Mag I	$U - B$	$\log F_{[\text{O III}]}$ (erg/s/cm ²)	$\log F_{\text{H}\beta}$ (erg/s/cm ²)	$\log([\text{O III}]/\text{H}\beta)$	Survey (3)	Classification (4)
277		13049199	215.39731	53.14485	0.5716	21.64	0.92	-16.65 ± 0.13	-16.90 ± 0.15	0.30	1	AGN-2
278		13049743	215.23357	53.15166	0.6715	21.20	0.90	-15.85 ± 0.17	< -16.42	> 0.58	2	AGN-2
279	egs_0917	13050479	215.16222	53.13790	0.6873	21.22	1.24	-15.45 ± 0.03	-16.29 ± 0.10	0.87	1	AGN-2
280		13050506	215.13316	53.16930	0.7175	21.78	1.11	-16.22 ± 0.10	-16.42 ± 0.10	0.21	1	AGN-2
281		13050545	215.18217	53.16978	0.8066	20.77	1.25	-16.30 ± 0.10	-16.77 ± 0.18	0.41	1	AGN-2
282		13050592	215.16920	53.14497	0.5497	20.21	0.99	-15.95 ± 0.06	< -16.79	> 0.88	1	AGN-2
283	egs_0899	13050600	215.13885	53.13954	0.7380	18.88	1.34	< -15.25	< -15.45	...	2	XBONG
284		13051178	215.04519	53.14959	0.6878	21.77	0.60	-15.69 ± 0.13	< -16.21	> 0.73	2	AGN-2
285		13051207	215.04222	53.12734	0.5747	20.29	1.15	-15.45 ± 0.04	-16.06 ± 0.07	> 0.60	1	AGN-2
286		13051923	215.00124	53.12522	0.3537	18.62	1.28	-16.08 ± 0.11	< -16.48	> 0.40	1	AGN-2
287		13051924	215.01083	53.12492	0.3531	18.96	1.23	-16.46 ± 0.14	< -16.78	> 0.33	1	AGN-2
288		13055483	215.61987	53.23400	0.6946	21.14	0.94	-16.21 ± 0.20	< -16.57	> 0.32	2	AGN-2
289		13056236	215.57861	53.19849	0.7011	21.39	1.17	-15.74 ± 0.06	-16.34 ± 0.13	0.57	1	AGN-2
290	egs_1114	13056732	215.47356	53.23130	0.6720	20.50	1.02	-15.37 ± 0.02	-16.38 ± 0.07	1.02	1	AGN-2
291		13056838	215.50259	53.18146	0.6782	21.00	1.24	< -16.74	< -17.05	> 0.28	1	AGN-2
292		13056845	215.44473	53.23426	0.6721	20.30	1.14	-16.56 ± 0.20	< -16.82	> 0.28	1	AGN-2
293		13056869	215.42471	53.21977	0.6793	20.64	1.34	-16.71 ± 0.16	< -17.07	> 0.36	1	AGN-2
294	egs_1136	13056914	215.50252	53.19047	0.5609	19.25	0.99	< -16.19	< -16.47	...	2	XBONG
295		13058008	215.31335	53.18832	0.7087	21.06	1.14	-15.30 ± 0.02	-16.27 ± 0.12	> 0.99	1	AGN-2
296		13058102	215.25298	53.20337	0.3827	19.74	1.22	-16.72 ± 0.18	< -17.00	> 0.29	1	AGN-2
297		13058131	215.24632	53.18076	0.7139	21.42	1.23	-16.71 ± 0.21	< -16.87	> 0.15	1	AGN-2
298		13058183	215.27882	53.22486	0.3921	20.60	1.12	-16.51 ± 0.15	< -16.86	> 0.34	1	AGN-2
299	egs_0968	13058235	215.23860	53.18446	0.7136	21.49	1.21	-15.84 ± 0.03	-16.66 ± 0.10	0.85	1	AGN-2
300		13058752	215.13882	53.18595	0.6771	20.38	1.27	-16.43 ± 0.18	< -16.74	> 0.31	1	AGN-2
301		13058803	215.21223	53.20697	0.6374	20.33	1.29	-16.33 ± 0.13	< -16.94	> 0.40	1	AGN-2
302		13058823	215.20148	53.19695	0.5560	21.26	1.11	-16.32 ± 0.10	< -16.89	> 0.60	1	AGN-2
303		13058839	215.17076	53.18364	0.3547	18.64	1.27	-16.14 ± 0.09	-16.41 ± 0.13	> 0.28	1	AGN-2
304		13059384	215.08408	53.23315	0.4695	20.63	1.23	-16.43 ± 0.20	< -16.76	> 0.39	2	AGN-2
305	egs_1195	13062928	215.61546	53.23870	0.7292	21.75	1.20	< -16.28	< -16.34	...	2	XBONG
306		13063197	215.65708	53.24151	0.7545	20.81	1.25	-15.81 ± 0.13	< -16.61	> 0.78	2	AGN-2
307		13063488	215.56953	53.24950	0.6060	20.01	1.02	-15.87 ± 0.10	< -16.28	> 0.40	1	AGN-2
308	egs_1174	13063578	215.58286	53.25450	0.6361	20.22	0.78	-15.58 ± 0.02	-15.39 ± 0.02	-0.14	1	AGN-1
309		13063707	215.46152	53.24840	0.7101	20.98	1.19	-16.47 ± 0.16	< -16.63	> 0.16	1	AGN-2
310	egs_1081	13063920	215.42412	53.25177	0.5589	20.29	0.59	-16.04 ± 0.05	-15.69 ± 0.02	-0.34	1	SF+AGN
311		13064305	215.35243	53.25941	0.4453	19.42	1.09	-16.51 ± 0.20	< -16.85	> 0.33	1	AGN-2
312	egs_1071	13064321	215.40923	53.24750	0.6695	21.51	1.22	-16.70 ± 0.14	-17.11 ± 0.20	0.46	1	AGN-2
313		13064472	215.31825	53.26095	0.7405	21.63	1.23	-16.13 ± 0.04	-16.82 ± 0.10	0.68	1	AGN-2
314	egs_0747	13101998	214.91539	52.91878	0.7546	21.20	0.79	-15.54 ± 0.02	-16.07 ± 0.03	0.50	1	AGN-2
315		14001330	215.80038	53.24900	0.7674	21.29	0.84	-15.98 ± 0.14	< -16.45	> 0.64	2	AGN-2
316		14005533	215.75452	53.31112	0.6813	20.52	1.21	-16.43 ± 0.14	-16.56 ± 0.11	0.11	1	AGN-2
317		14005765	215.75554	53.27140	0.6803	20.26	0.85	-15.81 ± 0.21	-16.19 ± 0.20	> 0.40	2	AGN-2
318		14006154	215.68740	53.27952	0.7219	20.78	1.11	-15.89 ± 0.19	< -16.11	> 0.29	2	AGN-2
319		14006225	215.70694	53.31096	0.6344	19.73	0.97	-15.67 ± 0.08	-15.64 ± 0.07	-0.05	1	AGN-1
320		14006257	215.73434	53.28779	0.6858	21.27	1.14	-16.73 ± 0.17	< -17.02	> 0.31	1	AGN-2
321		14006702	215.56920	53.29696	0.4980	20.21	1.09	-16.16 ± 0.06	-16.56 ± 0.13	0.42	1	AGN-2
322		14006727	215.57568	53.27760	0.3562	19.01	2.06	-15.63 ± 0.04	-16.01 ± 0.06	0.37	2	AGN-2
323	egs_1102	14007146	215.45893	53.31067	0.5736	20.20	1.27	< -15.90	< -16.32	...	2	XBONG
324		14007176	215.53458	53.29059	0.4306	19.50	1.18	-16.21 ± 0.09	-16.55 ± 0.16	0.33	1	AGN-2
325		14007560	215.42955	53.30557	0.7653	20.94	1.17	-15.78 ± 0.04	-16.62 ± 0.12	0.84	1	AGN-2
326		14007624	215.40796	53.28931	0.4505	20.14	1.26	-16.44 ± 0.11	-16.41 ± 0.07	-0.01	1	AGN-2
327	egs_1075	14007649	215.41282	53.26965	0.3509	20.42	1.05	-15.71 ± 0.04	-16.45 ± 0.10	0.72	2	AGN-2
328		14007947	215.33629	53.29414	0.6875	21.60	1.02	-16.28 ± 0.06	< -17.08	> 0.79	1	AGN-2
329	egs_0984	14007988	215.26402	53.30631	0.7088	20.50	0.54	-15.84 ± 0.04	-16.27 ± 0.06	0.41	1	AGN-1
330	egs_1041	14008025	215.34576	53.31094	0.5731	19.29	1.24	< -16.16	< -16.41	...	1	XBONG
331		14010918	215.84533	53.32498	0.4073	18.38	1.15	-15.95 ± 0.18	-16.05 ± 0.16	0.08	2	AGN-2
332		14011211	215.81438	53.33645	0.6024	21.00	1.20	-16.72 ± 0.20	-17.14 ± 0.20	0.33	1	AGN-2
333		14011283	215.77611	53.36661	0.6149	20.42	1.42	-16.85 ± 0.20	< -17.02	> 0.15	1	AGN-2
334	egs_1206	14011813	215.65298	53.36228	0.7697	20.65	1.03	-15.57 ± 0.02	-16.02 ± 0.03	0.46	1	AGN-2
335		14012248	215.56296	53.35854	0.7653	21.30	1.37	-16.87 ± 0.21	< -17.20	> 0.30	1	AGN-2
336	egs_1196	14012314	215.61560	53.38070	0.3554	19.29	1.06	-16.28 ± 0.18	-16.21 ± 0.10	-0.08	2	SF+AGN
337	egs_1103	14012868	215.45920	53.34058	0.6710	20.53	1.13	-16.24 ± 0.10	-16.45 ± 0.10	0.21	1	AGN-2
338	egs_1097	14013393	215.45317	53.34676	0.6716	20.17	1.38	-16.16 ± 0.10	< -16.69	> 0.53	1	AGN-2
339		14013542	215.29845	53.32955	0.7662	21.01	0.97	-16.61 ± 0.13	-16.88 ± 0.13	0.28	1	AGN-2
340	egs_1015	14013811	215.31638	53.33019	0.4272	20.81	0.63	-15.58 ± 0.02	-16.25 ± 0.05	0.70	1	AGN-2
341		14014263	215.25688	53.36148	0.5696	19.46	1.03	-15.65 ± 0.20	< -15.94	> 0.28	2	AGN-2
342		14016536	215.89078	53.41935	0.7834	21.62	1.36	-16.65 ± 0.20	< -16.75	> 0.05	1	AGN-2
343		14016630	215.85455	53.43721	0.4430	19.86	1.26	-16.34 ± 0.09	< -16.90	> 0.53	1	AGN-2
344		14016667	215.86427	53.40709	0.7672	20.73	1.06	-15.33 ± 0.02	-16.09 ± 0.04	0.86	1	AGN-2
345	egs_1293	14017079	215.82256	53.42390	0.6310	20.20	1.07	< -16.41	< -16.36	...	1	XBONG
346	egs_1244	14017382	215.70819	53.38271	0.4428	20.86	1.08	-16.08 ± 0.10	-16.02 ± 0.06	-0.04	2	SF+AGN
347	egs_1207	14017523	215.65463	53.43590	0.5114	20.30	0.84	-15.35 ± 0.01	-15.81 ± 0.02	0.45	1	AGN-2

Continued on Next Page...

EGSAGN No	LNG2009 ID (1)	DEEP2 ObjNo (2)	RA (J2000)	Dec	z	Mag I	$U - B$	$\log F_{[\text{O III}]}$ (erg/s/cm ²)	$\log F_{\text{H}\beta}$ (erg/s/cm ²)	$\log([\text{O III}]/\text{H}\beta)$	Survey (3)	Classification (4)
348		14018001	215.61223	53.42194	0.3555	19.12	1.12	-16.67 ± 0.20	< -16.84	> 0.19	1	AGN-2
349		14018380	215.51559	53.43000	0.7878	21.98	0.72	-15.78 ± 0.05	-16.41 ± 0.12	> 0.73	1	AGN-2
350		14018776	215.38621	53.38613	0.6371	20.84	1.10	-15.96 ± 0.14	< -16.39	> 0.37	2	AGN-2
351		14018802	215.42799	53.42478	0.6364	21.72	1.24	-16.86 ± 0.18	< -16.99	> 0.11	1	AGN-2
352		14018805	215.43602	53.41988	0.6367	21.17	1.10	-16.67 ± 0.15	< -16.90	> 0.21	1	AGN-2
353		14018830	215.43962	53.38706	0.6188	22.00	1.18	-16.75 ± 0.19	< -16.80	> 0.05	1	AGN-2
354		14018925	215.40747	53.38294	0.7611	20.56	1.02	-16.40 ± 0.18	< -16.70	> 0.36	1	AGN-2
355		14022036	215.95416	53.44591	0.4087	19.30	1.11	-15.87 ± 0.07	< -16.49	> 0.66	1	AGN-2
356	egs_1267	14022888	215.76204	53.43998	0.6156	19.97	0.73	-15.68 ± 0.07	-15.52 ± 0.05	-0.12	1	SF+AGN
357		14023340	215.65662	53.47221	0.5091	20.40	1.26	-16.41 ± 0.10	-16.66 ± 0.14	0.24	1	AGN-2
358		14023725	215.63082	53.44194	0.6356	21.37	0.88	-15.95 ± 0.10	-16.36 ± 0.16	0.40	2	AGN-2
359		14024142	215.51714	53.47835	0.3574	19.75	0.95	-15.87 ± 0.07	-16.15 ± 0.09	0.28	2	AGN-2
360	egs_1095	14024634	215.44897	53.47337	0.6040	20.47	1.15	-16.04 ± 0.06	-16.37 ± 0.11	0.35	1	AGN-2
361	egs_1306	14028007	215.85330	53.51669	0.7697	20.46	1.43	< -16.46	< -16.71	...	1	XBONG
362		14028114	215.87643	53.50116	0.3500	18.85	1.32	-16.36 ± 0.11	< -16.74	> 0.39	1	AGN-2
363		14028159	215.85008	53.51573	0.4417	19.68	1.29	-16.54 ± 0.11	< -16.97	> 0.41	1	AGN-2
364	egs_1263	14028502	215.75780	53.54840	0.4133	19.14	1.04	-15.88 ± 0.06	-16.15 ± 0.10	0.26	1	AGN-2
365		14028987	215.72119	53.53766	0.7416	20.67	1.19	-16.82 ± 0.21	< -17.05	> 0.22	1	AGN-2
366		14029001	215.69868	53.52681	0.6421	21.74	1.29	-16.68 ± 0.15	< -16.86	> 0.18	1	AGN-2
367		14029014	215.68240	53.51499	0.4569	18.59	1.19	-16.28 ± 0.14	< -16.69	> 0.41	1	AGN-2
368	egs_1193	14029471	215.61250	53.50137	0.4854	19.36	1.00	-15.38 ± 0.02	-15.77 ± 0.04	0.44	1	AGN-2
369		14034717	215.74310	53.55619	0.7406	21.77	0.97	-16.68 ± 0.21	< -16.87	> 0.30	1	AGN-2
370		14034728	215.71265	53.60481	0.3868	18.77	1.21	-15.36 ± 0.02	-16.72 ± 0.22	1.38	1	AGN-2
371	egs_1189	14035190	215.60696	53.57407	0.7576	20.17	0.71	-15.82 ± 0.06	-16.01 ± 0.04	0.17	1	AGN-1
372		14035196	215.56306	53.56962	0.4132	19.89	1.18	-16.41 ± 0.16	< -16.50	> 0.10	1	AGN-2
373		14035205	215.64598	53.56277	0.4138	18.87	1.20	-16.10 ± 0.19	< -16.25	> 0.16	2	AGN-2
374	egs_1292	14100240	215.82221	53.31287	0.5142	21.44	0.61	< -16.45	-16.57 ± 0.21	< 0.12	2	AGN-1

(1) ID in (Laird et al. 2009). X-ray undetected sources have no ID.

(2) DEEP2 object number; see <http://deep.berkeley.edu/DR1/photo.primr.html>.

(3) Source of the redshift, [O III], and H β measurements: 1 – DEEP2, 2 – MMT/Hectospec follow-up.

(4) Classifications: AGN-1 = Type 1 AGN; AGN-2 = optically selected Type 2 AGN, including both X-ray detected and undetected; SF+AGN = X-ray loud, composite galaxies; XBONG = X-ray Bright, Optically Normal Galaxies; Gal = X-ray detected normal galaxies; Ambiguous = X-ray sources with ambiguous optical classifications; Blended = known cases of blended objects for which the optical spectrum and the X-rays are from different objects.

(5) DEEP2 Object 11027275 is a B-band drop out; its U-B color is not available.